UNIVERSITY OF SOUTHAMPTON

# Smart viscoelastic supports for vibration control in rotors

by

A. A. Zakaria

A thesis submitted in partial fulfillment for the
degree of Master of Philosophy

in the
The Faculty of Engineering and Physical Sciences
Institute of Sound and Vibration Research

March 2023

UNIVERSITY OF SOUTHAMPTON

ABSTRACT

FACULTY OF ENGINEERING AND PHYSICAL SCIENCES
INSTITUTE OF SOUND AND VIBRATION RESEARCH

Master of Philosophy

# SMART VISCOELASTIC SUPPORTS FOR VIBRATION CONTROL IN ROTORS

by A. A. Zakaria

One of the most important operating requirements of rotating machinery is the capability to operate away from its critical speeds. It can be achieved by associating a material that has property variation when induced by external stimuli. The focus of this work is the application of smart viscoelastic to the rotor dynamics field by employing magneto-rheological elastomer (MRE) as its support. Characterisation of MRE property is determined through impact hammer test with and without the presence of a magnetic field. The modulus of the MRE was estimated from the accelerance FRF plot and compared with the MRE model. The MRE model is based on the inter-particle interaction in the rubber matrix and linearised with the assumption of small displacement around the equilibrium position of the particle. The model of magnetic field-dependent behaviour is combined with the viscoelastic property of the MRE in a series configuration. The linearised MRE model was fairly accurate to estimate the data from the hammer test and experimental data from the literature. Then a rigid rotor model, supported by a flexible mount at both ends that consist of plain bearing with the linearised MRE model is considered. The MRE support is simulated with a three-parameter standard linear viscoelastic model with the inclusion of induced magnetic field property. The simulation results, which were limited to zero-field conditions, indicate that the use of MRE in conventional bearing supports can shift the critical speeds and reduce its corresponding vibration amplitude. These results suggest that the critical speed shift due to the increase of ferromagnetic particles in MRE can be explored further, especially with the influence of the induced magnetic field.

# Contents

# List of Figures

# List of Tables

# Nomenclature

| | |
|---|---|
| $\rho_{cip}$ | Density of carbonyl iron particle (CIP) |
| $\rho_{sr}$ | Density silicone rubber |
| $m_f$ | Mass of final mixture of silicone rubber and CIP |
| $\phi$ | Volume percentage of CIP |
| $\upsilon_{cip}$ | CIP volume |
| $\upsilon_{sr}$ | Silicone rubber volume |
| $m_{eff}$ | Effective mass of SDOF test setup |
| $m_{steel}$ | Mass of cylindrical steel |
| $m_{MRE}$ | Mass of MRE sample |
| $k_{MRE}$ | Stiffness of MRE sample |
| $\omega_n$ | Natural frequency from maximum accelerance |
| $\omega_a$ | Left side adjacent frequency of Nyquist plot |
| $\omega_b$ | Right side adjacent frequency of Nyquist plot |
| $\theta_a$ | Angle in radian between $\omega_a$ and $\omega_n$ |
| $\theta_b$ | Angle in radian between $\omega_b$ and $\omega_n$ |
| $\eta$ | Loss factorof MRE sample |
| $k_1$ | Estimated MRE stiffness $k_{MRE}$ using Equation (3.3) |
| $k_2$ | Estimated MRE stiffness $k_{MRE}$ using Equation (3.4) |
| $k_B$ | Linearised MRE stiffness using Equation (5.10) |
| $d$ | Diameter of spherical CIP |
| $r_0$ | Initial gap between evenly distributed CIP |
| $h$ | Reciprocal indicator of CIP distance |
| $E$ | Interaction energy between two dipoles |
| $M$ | Magnetic dipole moment |
| $r$ | Distance between two adjacent dipole |
| $\mu_0$ | Space permeability |
| $\mu_1$ | MRE permeability |
| $\varepsilon$ | Scalar strain of dipoles |
| $U$ | Energy density or interaction energy between dipoles per unit volume |
| $\sigma$ | Stress induced by magnetic field |
| $J_p$ | Average particle polarization |
| $V$ | Volume of MRE elementary cell |

| | |
|---|---|
| $G$ | Shear modulus of MRE |
| $B$ | Applied magnetic field |
| $B_s$ | Saturation flux density |
| $J_s$ | Saturation of polarization |
| $H$ | Magnetic field strength |
| $k$ | Fitting parameter |
| $E_{mag0}$ | Modulus of MRE without magnetic field |
| $E_{CIP}$ | Young's modulus of CIP |
| $E_{SR}$ | Young's modulus of silicone rubber |
| $E_{mag}$ | Linearised magnetic Young's modulus |
| $\varepsilon_{eq}$ | Scalar strain dipoles around equilibrium position |
| $E_{MRE}$ | Total linearised MRE modulus |
| $m$ | Mass of rigid rotor |
| $XYZ$ | Cartesian coordinate axes |
| $x\dot{x}\ddot{x}$ | horizontal displacement, velocity, and acceleration of rotor center |
| $y\dot{y}\ddot{y}$ | vertical displacement, velocity, and acceleration of rotor center |
| $\Omega$ | Angular velocity |
| $\psi\dot{\psi}$ | Angular direction and velocity about $X$-axis |
| $\theta\dot{\theta}$ | Angular direction and velocity about $Y$-axis |
| $\epsilon$ | Rotor eccentricity |
| $\beta$ | Rotor skewed centerline angle |
| $I_d$ | Diametral moment of inertia |
| $I_p$ | Polar moment of inertia |
| $\delta$ | Initial condition of translational motion |
| $\gamma$ | Initial condition of rotational motion |
| $\mathbf{M}$ $\mathbf{C}$ $\mathbf{K}$ | Mass, damping, and stiffness matrices |
| $\mathbf{q}$ | DOF matrix |
| $s_n$ | Complex eigenvalues |
| $\zeta$ | Damping ratio |
| $\omega_d$ | Damped natural frequency |
| $k_B$ | Linearised MRE stiffness |
| $A$ | Cross-sectional area of MRE sample |
| $l$ | Length of MRE sample |
| $k_\infty$ | Stiffness constant |
| $\mathbf{w}(t)$ | Unbalance mass matrix |

# Declarations

I, AZRUL ABIDIN BIN ZAKARIA

declare that this thesis and the work presented in it are my own and has been generated by me as the result of my own original research.

Smart Viscoelastic Supports for Vibration Control in Rotors

I confirm that his work was done wholly or mainly while in candidature for a research degree at this university; where any part of this thesis has previously been submitted for a degree or any other qualification at this University or any other institution, this has been clearly stated; where I have consulted the published work of others, this is always clearly attributed; where I have quoted from the work of others, the source is always given. With the exception of such quotations, this thesis is entirely my own work. I have acknowledged all main sources of help; where the thesis is based on work done by myself jointly with others, I have made clear exactly what was done by others and what I have contributed myself.

Signed :
Date : 17th March 2023

## Acknowledgements

I would like to epxress my deepest gratitude to Assoc. Prof. Dr. Emiliano Rustighi and Dr. Neil Ferguson for their continuous supports, encouragement and ideas over the years. I am also grateful to join Dynamics Group that give me chance to meet new friends while finishing my study at Southampton. All your kind help especially during my time at Dynamics Lab will not be forgotten.

*To...*

*My caring parents who have raised me to the person I am*
*My wonderful wife whose sacrifice a lot for me and our daughters*
*My Rafa and Ruhi who are indeed priceless treasures from Allah*

# Chapter 1

# Introduction

## 1.1 Background

A viscoelastic material is known to be a good choice for use within an isolation system due to it being inexpensive and possessing high damping characteristics over a wide temperature and frequency range. In rotor dynamics applications, the dynamic problems that require solutions encompass reduction of any response due to unbalance and ensuring that the system does not become unstable at critical speeds by increasing instability thresholds. Tackling such issues are important requirements to prolong the lifespan of rotating machinery and increase their efficiency. In some of these dynamic scenarios isolation is an important passive vibration control solution, typically implemented using rubber bushing and elastomer supports. However, slight variations either in the environmental conditions or the parameter of the operating machine may contribute to changes in the isolation characteristics, as the viscoelastic material properties are both temperature and frequency-dependent. This complexity might be difficult to incorporate in any design or it can produce constraints on the optimum isolation performance. Hence it is necessary to develop the existing dynamic models to cope with such changes, producing more complex system dynamics and ultimately to improve the performance by considering the introduction of isolation material that can be adapted or semi-actively controlled. Hence the eventual need to consider, via modelling and ultimately implementation, is the introduction of smart viscoelastic supports which benefit from the required stiffness and damping but are robust to changing operating conditions.

## 1.2 Project Aims & Objectives

This project is being undertaken to advance the current application of viscoelastic supports in rotor systems by exploring the potential of novel smart material, such as the

magnetorheological elastomer (MRE). In order to maintain specific mechanical properties which provide required optimum vibration isolation performance, an adaptive or semi-active control system can be envisaged where the magnetic field applied to the MRE material can be altered. Then the MRE damping and stiffness properties, which might vary with temperature and frequency of the system, can be either corrected or changed. The focus of this project will initially be on mathematical modelling of rotor-dynamics systems, encompassing both rigid and then flexible rotors on elastic supports. The performance will be compared to the results given in existing literature and then the governing equations of motion will be developed to incorporate MRE supports and predictions of the behaviour for comparison with passive isolation supports. This will be accompanied by designing a test rig prototype of the support for model validation. Subsequently the project will consider the requirements and choice of the most appropriate control algorithms, their performance modelling and final implementation and proof of concept. Below is the list of main objectives to be achieved in this work:

- Determine the properties of MRE by modal testing through impact hammer test. The test is facilitated with stack of permanent magnet to induce magnetic field during the test.
- Determine the mathematical model of rotor-bearing system supported by MRE. The whole model comprised the MRE dependency properties on both without and with presence of magnetic field.
- Develop a rotor-bearing mathematical model supported by identical flexible mounts of smart viscoelastic supports.

### 1.2.1 Contributions

Below are contributions that have been determined throughout this work:

- An improvised impact hammer testing for obtaining complex stiffness properties of MRE is proposed. The setup will benefit the existing measurement devices and the and faster measurement time, using a modal testing method. Utilization of impact hammer test with consideration of single-degree-of-freedom system, MRE stiffness and lost factor can be determined from accelerance and Nyquist plot respectively. However, the test is only limited to a single excitation frequency whereas MRE, a viscoelastic material is a frequency dependent material.
- MRE properties of magnetic field dependency is modelled in compression for the first time using inter-particle or dipoles interaction. Simple compression deformation model of the MRE is determined from the shear model, where generally the shear model is widely used by other researchers. The model take into account zero-field elastic property of MRE by using series configuration of law of mixture. Then,

the magnetic dependent property of the model is linearly approximated using fifth order Taylor's series expansion of small strain around static equilibrium position. Both properties were combined to model linearised MRE modulus and stiffness.

- Effect of viscoelastic supports for rotor-bearing system is modelled by adapting the work done by [5]. Addition to the results presented by [5], potential of smart viscoelastic material as supports in rotor dynamics is highlighted in this work by demonstrating the material capability of reducing magnitude of vibration response and shifting its natural frequency.

# Chapter 2

# Literature Review

## 2.1 Introduction

In this chapter a brief literature review is presented to cover topics which include a glance into the history of rotordynamics, the modelling of viscoelastic material and viscoelastic material applications in rotordynamics. It is then followed by a specific review pertaining to magnetorheological elastomer behaviour and the controllability of material properties with respect to the magnetic field.

## 2.2 History of rotordynamics

Manufacturing of rotating machines began as early as the ancient Greek time. These machines were essential to provide energy from water flow to power other mechanical devices. Since then, it evolved to be one of main innovations in the power generation sector. During 1800s, great number of water mills were produced to generate power up until the beginning of the industrial revolution. Then, in the late 1800s, steam turbines became available for higher energy demands.

The earliest rotordynamic problem was the significance of the critical speed. It was the speed that amplified vibration generated from rotor unbalance by resonance at the natural frequency of the system. Thus, from the work of Rankine [6] in 1869 which analysed critical speed anomaly, most of the rotor-bearing system design was to retain its operational speed below the first critical speed. However, DeLaval [7] proved experimentally that it was possible to run above the critical speed in the supercritical region. As DeLaval [7] and Parsons [8] in the early 1900s managed to operate steam turbines at supercritical speed and since Jeffcott [9] successfully published a proper analysis of critical speed inversion with inclusion of damping, it became an acceptable practice for turbomachinery running in the supercritical region.

The influence of bearing properties became notably important with experiments on oil film bearings and its corresponding mathematical treatments in 1886 by Osborne Reynolds [10]. Previously bearings were just treated as a simple support with infinite stiffness. The main highlight of the work was that pressure generated by an oil film, which was due to rotation of the bearing journal, produces a force that is ample enough to support the load and prevent metal contact between bearing and shaft. The finding gave useful insight of the initial thought that the purpose of oil film in the first place was just to minimize friction between shaft and bearing.

Apart from the issues with critical speed and influence of bearing properties, shaft related problems were found to be a major concern in rotordynamics. In early 1900s, Newkirk [11] and Kimball [12] first addressed whirl instability from several experiments and the related theoretical analysis performed by Smith [13]. The instability was caused by subsynchronous whirling of the shaft. Then, the subsequent works explained the whirling phenomenon caused by internal friction or damping in the rotor assembly.

These issues, either the expansion of a single one or combinations of them, later on became the foundation of modern rotordynamics advancement. It leads to notable inventions, solutions and explanations that try to overcome the issues. Development of a squeeze film bearing damper, as an example, is a well known type of bearing that invented to facilitate high rotation devices such as a helicopter shaft [14], a flow compressor in aircraft engines and the turbojet [15] by the 1970s.

As time progressed, the need for power and speed for rotating machinery were becoming prominent. Multiple stage turbines and compressors, and the rocket engine are examples of such devices that require precise analysis in terms of the instability of subsynchronous whirl and balancing. Because of these problems, most development over the last several decades in rotordynamics focused on bearings and seals for vibration damping devices, and tools for analysis and measurements [16].

## 2.3 Viscoelastic material modelling and characteristics

Over a century ago, interest in viscoelastic material and its application grew tremendously. Starting with a mathematical representation of viscoelastic models such as the Maxwell, Kelvin-Voigt (KV) and standard linear model. Maxwell and KV models are visualized by connecting a Hookean spring with Newtonian damper in series and parallel respectively. In general the Maxwell model is acceptable as a first approximation to relaxation behaviour, but is inadequate for prediction of creep (strain increases linearly with time) and recovery (instantaneous recovery of elastic strain when stress is removed). However, the KV model is acceptable as a first approximation to creep and recovery behaviour, but is inadequate for prediction of relaxation due to stress-relaxation relation. When the stress is constant, the predicted response shows the material behaves as an

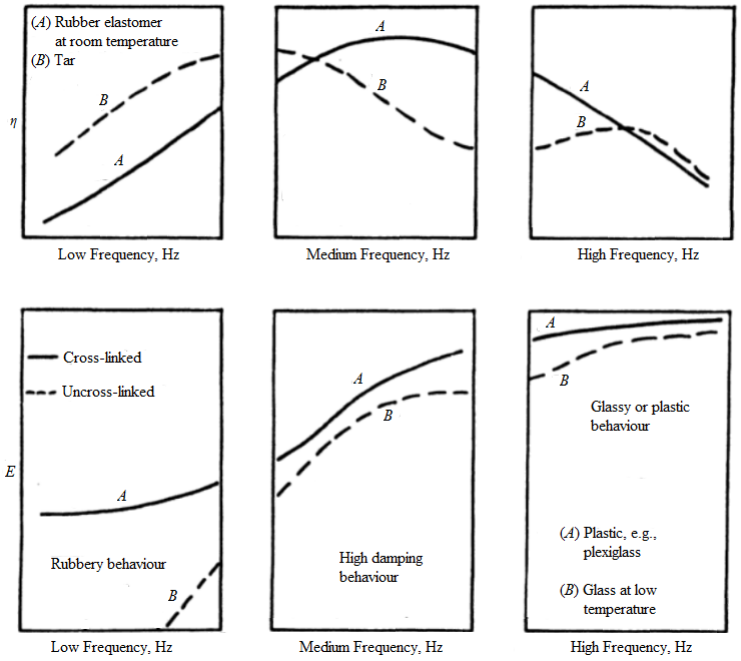


FIGURE 2.1: The effect of increasing frequency on the storage modulus and loss factor for four materials at constant temperature [1].

elastic solid. The restrictions of the two models can be overcome by combining the two models into a standard linear solid model.

Numerous publications advanced the development of the material modelling to accurately reproduce the viscoelastic characteristics. Important work is presented below. Among the earliest advancement of mathematical modelling of viscoelastic material was the utilization of fractional calculus [17]. The idea of fractional integration and differentiation are used for the derivation of a new fundamental equation for viscoelastic materials. Good agreement between theoretical and experimental results indicated that the concept gave advantages for describing viscoelastic properties, which utilize one parameter, compared to the traditional method, which requires more than one parameter to fit the experimental data.

One of the key features of viscoelastic material is its mechanical properties which vary with frequency and temperature. As an example, the frequency and temperature dependence effect on the storage modulus and loss factor of some viscoelastic materials are shown in Figure 2.1 and Figure 2.2 respectively.

In Figure 2.1, the effect of increasing frequency on four viscoelastic materials are illustrated at room and low temperature. These temperatures are selected to show the effect at the glassy, transition and rubbery regions. The storage modulus always increases as frequency increases, where a greater rate of change is observed in the transition region. For loss factor, it increases with increasing frequency, reaches a maximum value

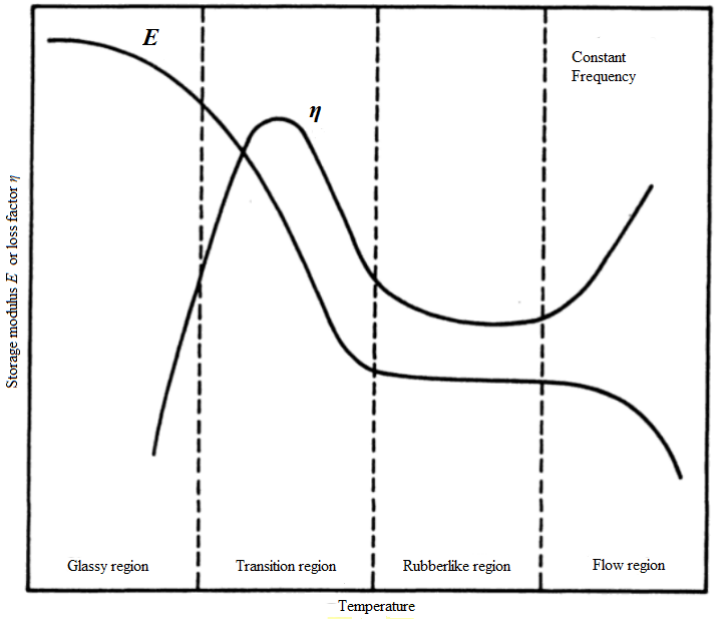


FIGURE 2.2: The effect of temperature on the storage modulus and loss factor for typical viscoelastic material with constant frequency [1].

in transition region and then decreases in the glassy region. Variation of storage modulus and loss factor in four distinct regions as temperature increases can be observed in Figure 2.2. In general [1], this figure shows that it is qualitatively the inverse of the frequency behaviour, but to a higher degree. It takes a few degrees of temperature to produce the same change of behaviour as a several decades of frequency. Thus, in order to facilitate the temperature dependence of viscoelastic material, Ketema and Fosdick [18] incorporate a fading characteristic into dynamic absorber. The fading characteristic is a time-temperature superposition method's function that governs the relaxation time dependence on temperature. An advantage of this model is that the dependency of temperature on the relaxation time can be used to tune the effectiveness of a dynamic vibration absorber.

Sjöberg and Kari [19] modelled the frequency dependence of viscoelastic properties of a non-linear rubber isolator in a dynamic system by a fractional calculus element. The model works in the time-domain and good agreement is obtained in a wide frequency and amplitude range for a freely oscillating one degree of freedom system. The model is found to be superior to the commonly applied Kelvin-Voigt element in modelling the dynamic isolator properties. Adolfsson et al. [20] discussed different formulations of the fractional order viscoelastic model and provided physical interpretations of the model by using viscoelastic functions. They showed that the fractional order model is equivalent to the standard viscoelastic model with an infinite number of internal variables in the sense that the models give the same stress response on a given strain history.

Silva et al. [21] showed how to make a time-varying controller sensitive to temperature changes for viscoelastic material. The work depicted how both the frequency and

temperature dependence of viscoelastic materials can be modelled with internal variables. Gil-Negrete et al. [22] proposed a material model that combines elastoplasticity and fractional order viscoelasticity to represent the complex behaviour of natural rubber mixtures by using an overlay technique. A fractional-derivative viscoelastic model maintained a low number of parameters and simplified the parameter fitting procedure. When subjected to harmonic excitation, von Mises' elastoplastic material model showed a good resemblance to the rate independent behaviour of rubber mixtures. Advantages of the proposed model are its capability to simulate the complex dynamic behaviour of carbon-black filled rubber elements and to replicate the material behaviour.

All reported viscoelastic models above were derived to solve specific conditions of the viscoelastic material. As in [17], [19] and [20] each model tried to explain the frequency dependency of viscoelastic properties, while [18] and [21] mentioned the effect of temperature in their models. From these models, which have specific importance, it leads to a concern for modelling viscoelastic material by distinct assumptions so that accurate and definite analysis can be done.

## 2.4 Application of viscoleastic materials in rotordynamics

In parallel with the advancement of modelling viscoelastic material, which help to describe the complexity of the material properties, the application of viscoelastic components in rotordynamics has generally increased as well. Dutt and Nakra [23] studied the threshold speed of a rotor system on viscoelastic supports. The standard linear model of the solid viscoelastic was considered as a support for identical plain journal bearings of single disc rotor system. From the stability analysis, the zone of stable speeds can be increased by the use of a low value of the primary support stiffness ratio (ratio of primary spring and shaft stiffness), high value of secondary support stiffness ratio (ratio of secondary spring and shaft stiffness) and optimum values of the primary damping ratio (ratio of primary damper and critical damping coefficient), secondary damping ratio and support mass ratio (ratio of secondary damper and critical damping coefficient).

Shabaneh and Zu [24] investigated both the free and forced vibration of a rotating disk-shaft system with linear elastic bearings mounted on viscoelastic suspensions. By utilizing a KV model for the viscoelastic support and a Timoshenko beam model for the shaft, they found that by increasing the viscoelastic stiffness, the fundamental and second natural frequencies increase as well.

Tilemma [25] utilized component mode synthesis (CMS), which has shown to be an efficient method for modelling rotor dynamics applications with viscoelastic bearing supports. CMS is applicable to viscoelastic FEM components provided that the equations of motion are written in a convenient linear form.

Friswell et al. [5] investigated the effect of an elastomer support on the dynamics of a rotating machine. The effect of frequency and temperature dependent modulus has been demonstrated by using the internal variable approach to model the viscoelastic material for the transient dynamic responses, and includes an energy dissipation model. It was shown that the dynamic characteristics of a machine change significantly with temperature because of the changes in the stiffness and damping characteristics of the elastomer.

Bavastri et al. [26] presented a convenient way to determine the Campbell diagram of a dynamic rotor system with bearings containing viscoelastic layers. The viscoelastic material employed in the bearings was modelled with four parameter fractional derivative model. It was shown that the use of viscoelastic materials in the bearings could be very effective in vibration and noise control.

The capability of the material tackling the critical speed issue in [23] and [24], and vibration attenuation in [5] and [26] indicates the promising potential of viscoelastic material in future rotordynamics applications.

## 2.5 Magnetorheological elastomer

The discovery of magnetorheological elastomer (MRE) in 1983 has shed some light on how to overcome the problems faced when using MR fluids [27]. When viewed structurally, MRE can be seen as a solid-state analogue to MR fluids. MRE is a class of solid that comprises a polymeric matrix with embedded ferromagnetic particles such as carbonyl iron. By introducing a current or magnet conducting particle into the liquid-form of the polymeric matrix solid, the mixture is then exposed to the intense magnetic field and left to cure and solidify to become an elastomer. Since its mechanical properties change instantly by the application of a magnetic field, the magnetorheological elastomer became a widely used material when it comes to controllable features.

Brigadnov and Dorfmann [28] conducted mathematical modelling of MRE by using the concept of the strain-energy functions. The derivation of the equations are based on a model of MRE confined by parallel top and bottom plates, which is subjected to shear deformation under the influence of a magnetic field normal to the plates. An acceptable agreement was achieved between the numerical simulation and experimental results. It was shown that the effect of the magnetic field is to stiffen the shear response of the material.

Lokander and Sternberg [29] investigated the effect of size and dispersion of iron particles on the performance of isotropic magnetorheological (MR) rubber. They found that MR rubber materials with large irregular particles have a large MR effect, which is a property of MRE that changed or induced by the influence of magnetic field, although

the particles are not aligned within the material. This is due to the low critical particle volume concentration of the particles. An identical effect is also found for materials with carbonyl iron, if the particles are poorly dispersed.

Blom and Kari [30] indicated that the magneto-sensitive effect of MR rubber is dependent on its amplitude and frequency. From experimental results, rubber samples in the audible frequency range showed that both the magnitude and loss factor of the shear modulus are strongly amplitude dependent. These results also concluded that introducing iron particles into the rubber increase its amplitude dependence over the entire frequency range.

Wang et al. [31] investigated the effects of interactions between carbonyl iron particles and the matrix, based on silicone rubber, on the performance of MRE on both the MR effect and mechanical properties. By utilizing silane coupling agents during mixing process, it was seen that there was an improvement in dispersion of the iron particles and the interaction between iron particles and the matrix, thus increasing the tensile strength of the MRE.

Stepanov et al. [32] conducted elongation, static and dynamic shear experiments to study MRE behaviour in the presence of a homogeneous magnetic field. It was been found that the elastic modulus increases as an external homogeneous magnetic field increases up to 0.3 T(Tesla). The presence of the effect of pseudo-plasticity has also been found, leading to an increase in the shear loss modulus of the MRE.

Chen et al. [33] described that addition of carbon black into the MRE matrix leads to a well-bound micro-structure and results in a high MR effect, low damping ratio and improved tensile strength. Deng and Gong [34] developed an adaptive tuned vibration absorber (ATVA) by utilizing MRE as its smart spring elements. From the theoretical and experimental result, the ATVA developed performed better in terms of shift-frequency and vibration absorption capability from 27.5 Hz to 40 Hz and up to 25 dB respectively.

Li et al. [35] worked on the influence of particle coating on MRE mechanical behaviour. It was found that MRE with carbonyl iron-poly methyl methacrylate (CI-PMMA) coating has a larger storage modulus, smaller loss factor and smaller Payne effect than that of the sample with only CI particles because PMMA coated particles are harder than the silicone rubber matrix. Hence there is a decrease in the relative motion, and an increase in the bond strength between the particles and matrix respectively.

Blom and Kari [36] utilized MR material in the form of a rubber bushing and investigated its property with the influence of frequency, amplitude and magnetic field. The frequency and amplitude dependent stiffness of the bushing are modelled based on geometric dimensions and shear modulus. From the results presented, it can be seen that the the stiffness of the bushing can be controlled over a large range due to the applied magnetic field strength.

Lejon and Kari [37] studied the influence of temperature, strain amplitude and magnetic field on MRE characteristics. As the dynamic strain amplitude is increased, the measurement indicated that a decrease in shear modulus amplitude occurred. By increasing the frequency and magnetic field strength, the shear modulus magnitude is found to increase as well. However, the measurements indicate that temperature is the most influential of the parameters as the material stiffens significantly when the temperature reaches the transition phase.

Ferromagnetic particles and magnetic field are two main aspects that differentiate MRE from viscoelastic material. By addition of iron particles as in [29], [30], [31], [33] and [35], the property of the rubber matrix is enhanced either through a MR effect, damping capacity or tensile strength. The influence of the magnetic field is also found to be a main features in characterization of MRE properties. Increase in modulus with induced magnetic field increases is reported in [28], [32] and [37]. Thus it leads to the possibility of controlling the MRE properties by application of magnetic field [36]. Overall, it shows that enhancement of a rubber matrix material can be made by adding iron particles for both without and with the presence of a magnetic field.

Recently, the work related to MRE and rotordynamics is presented by [38]. The magneto-rheological elastomer mount is modelled using the four-parameter viscoelastic model. By using the Rayleigh beam theory, the rotor bearing system is modelled using the finite element method with the inclusion of the gyroscopic effect and the shaft's internal damping. Main focus of the work is the investigation of the effect of the application of the magnetic field intensity on the vibration amplitude and the first critical speed. From the shown simulation results, the MRE supports is capable to reduce the rotor vibration response at the disk in the steady-state condition and in shifting the first critical speed. The results also shown that increasing magnetic field intensity decreases the first critical speed while increasing the unbalance vibration response of the rotor bearing system at the resonant speed.

In addition, a prototype actuator was designed by [39] that utilized MRE layers as the rotor-bearing mount. During the speed-up experiment of the rotor system, of which a constant voltage is applied, the MRE-based actuator was able to shift ciritcal speed of the rotor by 12.9 Hz. It was also found that the maximum of 23% reduction of rotor peak vibration when 8V is supplied to the actuator.

### 2.5.1 MRE modelling

Many efforts to model MREs properties have been seen which account for the elastic, viscoelastic and magnetic field dependency. The viscoelastic property is generally modelled by either a Maxwell or Voigt model or combination of both. Additional stiffness elements can be added to increase the accuracy of these models. Furthermore, most

of magnetorheological (MR) material models are developed using the idea of the interactions between adjacent magnetized filler particles. Due to an applied magnetic field, the filler particles within the magnetic field will be magnetized and the magnetic pole ends are formed at each particle. Thus, the interaction between magnetized particles or known as dipoles which will induce stress within the elastomer matrix and finally alter the MRE properties. By combining both viscoelastic and magnetic dependency models, a comprehensive characterization of MREs can be achieved.

Dipole-dipole magnetic particle interaction model was used firstly by Jolly et al. [40] to describe the increase in shear modulus as a magnetic field is applied in the same direction as the particle chains. The same model has been utilized also by Davis [41] and Shen et al. [42] for magnetic-field dependent behaviour, which try to explain the shear stiffness of MREs under magnetic fields but using different approaches for zero-field shear stiffness, namely a finite element model and hyper elastic rubber model respectively. Overall, under small strain condition, the dipole-dipole magnetic particle interaction model is efficient and mathematically concise.

Subsequently more complicated models, which are based on magnetic-mechanical microstructure, have been developed [43–52] to consider both zero-field and magnetic-field dependency. These models could include the Young's modulus of MRE as a magnetic field and applied force are in the same direction as the particle chains.

Nevertheless, limited literature covering viscoelastic properties of MREs are reported even though the damping behavior is essential for predicting their characteristics. Work by Chen et al. [53] and Li et al. [54] adopted the dipole-dipole model to describe the magnetic field dependency. The standard linear solid and viscoelastic interfaces model were utilized by Chen et al. [53] and Li et al. [54] to define zero-field dependency behavior respectively. As the magnetic fields increased, both studies found increases in the shear modulus, but ascending and descending changes in the loss factor were reported [53, 54] respectively.

### 2.5.2 MRE testing

After the modelling of MREs, physical assessments or experiments on MRE material are required to verify the models. Many experimental setups have been developed to assess properties of MREs under two conditions, namely the absence of a magnetic field, known as zero-field, and with the presence of a magnetic field. The main experimental tests for obtaining MRE properties are tension, compression and shear tests. Various samples of the MREs with different volume percentages of ferromagnetic particle were tested under different intensity of applied magnetic fields. Next, several work will be mentioned to address which type of experiment test are used to characterize MRE property.

For shear tests, Shen et al. [42] utilized two types of rubber as main the elastomer matrix namely natural rubber and polyurethane. Higher MR effects is observed for MREs made of polyurethane when magnetic field is applied up until 395 mT. Stepanov et al. [32] performed the same test on MREs made of vinyl rubber with 23.9% volume of CIP. Similar trends for the MR effects were found as the applied magnetic field is increased. Specifically, 750% and 150% relative MR effects were achieved at small and 10% strain respectively. Opie and Yim [55] and Choi [56] conducted dynamic shear test at a maximum strain level of 10% and 20% respectively. Both studies found that at larger strains level, the MR effects were decreased. Yu and Wang [57] created silicone rubber MRE sample that has copper wire inside it to generate a magnetic field. Increases in the MR effects were found at about 77% and 15% in the small and large strain region respectively. Furthermore, utilizing a dynamic shear test, Zając et al. [58] and Hu et al. [59] reported a similar trend for the MR effects by explaining changes of the area enclosing the stress-strain hysteresis, and storage and loss moduli respectively.

For compression tests, Kallio [4] utilized a ring-shaped solenoid around a MRE sample that made of silicone rubber with 30% volume CIP. A magnetic field induction up to 1 T was achieved using such a solenoid. From the stress-strain curves with maximum strain level of 2%, 100% relative MR effect was found when a 0.7 T field was applied. Varga et al. [60] performed a compression test with a sample made of silicone rubber and 5.45% volume of CIP. The test was conducted to investigate the effect of the applied magnetic field direction on MR effects. An anisotropic sample with particle alignment parallel to applied magnetic field and loading direction was found to have highest MR effect of 58% increase in the shear modulus. Boczkwoska et al. [61] utilized polyurethane gel as an elastomer matrix with a maximum 30% volume particles as shear test samples. MR effects achieved in that work were reported at a very low level of 4.5% compared to other experiments. Guðmundsson [62] manufactured both anisotropic silicone rubber and polyurethane MREs for uniaxial shear stress. From the results of MR effects and moduli against strains, silicone rubber MRE possesses highest MR effects. Gordaninejad et al. [63] also performed compression test up to 20% strain for silicone rubber matrix with a maximum 23.9% volume particles. From the results of compressive modulus against strain, a decreasing trend of modulus is found as the strain increased for both zero-field and induced magnetic field.

For tensile tests, Stepanov et al. [32] also prepared vinyl rubber MRE samples with iron particle sizes ranging from 2 to 70 $\mu$m. From stress-strain results, 3000% relative MR effects are reported in the small strain region with an applied magnetic field of 0.35 T. The high MR effect is due to a low zero-field modulus of MRE. Bellan and Bossis [64] also performed tension tests using silicone rubber MRE samples with 15% volume particles. Results were presented as a stress difference rather than moduli difference, where the increase in stress due to the applied magnetic field can be found in the small strain region up to a maximum value of 5%.

To conclude the literature on MRE experiments, a maximum strain level reported was up to 120% [57], 40% [60] and 60% [32] for shear, compression and tension test respectively. In term of zero-field moduli tested, a maximum of 7.2 MPa [57], 4.5 MPa [62] and 530 kPa [64] were reported for shear, compression and tension test respectively. Highest relative MR effects of 3000% are achieved in [32], which performed in tension test and the magnetic field is at 0.35 T. When the relative value compared to absolute value of MR effects, it is still within the range of reported literature. Besides, a highest absolute MR effects of 5.3 MPa is observed in [62] with applied magnetic field of 0.7 T and as it is converted to relative value, the effects are well within the range of other literature. Therefore, consideration of both the absolute and relative MR effects is important when interpreting the experimental results. In general, MR effects are increased as the applied magnetic fields are increased. However, saturation appears at a certain level of the magnetic field, which is reported at 0.7 T as in [4] and [63]. A low zero-field modulus of MRE is reported to have higher relative MR effects [32], but not necessarily for absolute MR effects [62]. Generally, MREs with a higher percentage volume of iron particles will have greater MR effects.

## 2.6 Conclusions

This review gives an useful insight into several aspects of viscoelastic material such as its modelling development, corresponding characteristics typically temperature and dependence, and its application in rotordynamics. It also provides a possibility of employing smart materials as supports for rotor-bearing system as it can provide optimum vibration isolation performance through adaptive or semi-active control system. Therefore, a review on MRE, whose properties can be altered with application of a magnetic field, was conducted so that its behaviour can be well understood. The information covered so far will now be used in the next chapter for mathematical modelling and obtaining numerical results.

# Chapter 3

# MRE Manufacture and Testing

In this chapter, two main subsections on MRE fabrication and testing method for characterizing its property are presented. Materials, mixing details and manufacturing process for producing MRE will be presented first. Then it will follow by short review on type of material testing for MRE. After that details on modal testing on MRE samples will be explained.

## 3.1 MRE manufacture

MREs are considered as smart materials due to their capability of changing under the application of a magnetic field. In general, MREs are made of three main components: a rubber or elastomer matrix, ferromagnetic particles and additives. All of the materials are mixed together, placed into moulds and cured, with or without the presence of a magnetic field for anisotropic and isotropic samples respectively. In addition, applying heat to the mixture can accelerate the curing process.

Most researchers use silicone rubber as matrix, because it is easy to use and possesses good properties such as very good chemical and UV resistance, and exhibits a wide range of temperature performance [3]. The characteristic properties of MREs are mainly dependent upon the ferromagnetic particles that are embedded inside the matrix when external magnetic field is applied. Due to magnetization of the filler magnetic particles, the material property of MRE is influenced by the interaction between the particles. If an external load is applied to the material, three-dimensional crosslinks formed by the particles try to retain their condition and the same trend is proportional to the intensity of the magnetic field [65]. Generally, the main criteria required for the selection of the magnetic particles are low remnant magnetization and high permeability. Low remnant particles will ensure a reversible MR effect can be achieved. Otherwise, due to residual magnetic effects upon the magnetic field removal this will make particles keep attracting

TABLE 3.1: Properties of cured silicone rubber MM228 provided by ACC Silicones Ltd.

| **Property** | **Value** |
|---|---|
| Viscosity | 18000 mPa.s |
| Young's modulus | 0.62 MPa |
| Tensile strength | 5.06 MPa |
| Density | 1120 kg/m$^3$ |
| Hardness | 28°Shore A |
| Elongation at break | 5.06 MPa |

each other [29]. The high permeability property of the magnetic particle is required because such a property will make particles easily attracted by the applied magnetic fields and thus encourages a maximum MR effect [4].

Additives are normally required in manufacturing MREs, as they can improve the mixture. Silicone oil is frequently used as the additive to reduce viscosity in the uncured mixture, so that it will help dispersion of the magnetic particles. Apart from filling gaps between the particles and the matrix, the additives could level the distribution of the internal stress inside the MRE [66].

### 3.1.1 Materials

In this study, a silicone rubber kit has been provided by ACC Silicones Ltd. The MM288 silicone rubber kit comprises two components, namely the rubber and the hardener as part A and B respectively. Both are mixed together with the ratio A:B = 10:1. The kit can be cured at room temperatures within 24 hours, but the curing process can be accelerated by heating. A maximum of 30 minutes is required for the curing process if the applied heating temperature is 100°C. Mechanical properties of the raw silicone rubber are listed in Table 3.1.

As most researchers utilized silicone oil as an additive to reduce the uncured product and the final modulus of cured elastomer, no additive is required in this work during the mixing process. The viscosity of the silicone rubber is relatively low compared to [3] and it was also recommended by the provider that no additive is required for the MM228 kit.

Ferromagnetic particles used in this work were provided by BASF SE. Carbonyl Iron Powder (CIP) Type SQ is soft iron powder with particles having an average diameter of 5 $\mu$m. The iron powder consists of fine, grey particles which are spherical in shape. It has 99.5% purity of iron content. Iron particles are the best option for the magnetic particles in MREs because of their low remnant magnetization, high permeability and high saturation magnetization [29]. Due to these properties, high MR effects can be obtained as a result from better inter-particle interaction [67]. The properties of CIP are shown in Table 3.2 below.

TABLE 3.2: Properties of carbonyl iron powder (CIP) Type SQ provided by BASF SE.

| **Property** | **Value** |
|---|---|
| Particle diameter | 5 $\mu$m |
| Iron content | 99.5 % |
| Carbon content | 0.5 % |
| Density | 7874 kg/m$^3$ % |

### 3.1.2 Component amounts for mixing MRE raw materials

Specific amount of each material, as introduced in the previous section, has to be set prior to manufacture of the MRE. The desired percentage of ferromagnetic particles can be decided first, then the amount of two components of silicone rubber can be determined as the final MRE samples will be categorized with its specific ferromagnetic volume fraction. The volume fraction is calculated by specifying the total weight of the overall mixture, and given the density of both ferromagnetic particles and two component silicone rubber, the weight of each material can be determined. By setting the final weight of overall mixture, it is easier for the mixing process because weighing material can be done directly on a weighing scale. The density of the carbonyl iron particle, $\rho_{cip}$, and the silicone rubber, $\rho_{sr}$, are 1120 kg/m$^3$ and 7874 kg/m$^3$ respectively. For an example, the mass of final mixture is set to be $m_f$ and the volume percentage of CIP is $\phi$. By solving the simultaneous equation below,

$$\begin{aligned} \rho_{cip}\upsilon_{cip} + \rho_{sr}\upsilon_{sr} &= m_f \\ (1-\phi)\upsilon_{cip} - \phi & \\ upsilon_{sr} &= 0 \end{aligned} \tag{3.1}$$

the volumes of carbonyl iron particle, $\upsilon_{cip}$, and the silicone rubber, $\upsilon_{sr}$ can be obtained. Then its corresponding mass can be calculated by multiplying by its corresponding density. For silicone rubber, the calculated mass will be divided according to 10:1 ratio of Part A and Part B respectively. Table 3.3 indicates the amount used to manufacture MRE samples in this work.

TABLE 3.3: Amount of each material used in the manufacture of the MRE in this work

| $\phi$ (%) | **Mass (g)** | | | **Total mass (g)** |
|---|---|---|---|---|
| | Part A | Part B | CIP | |
| 10 | 153.1186 | 15.3119 | 131.5696 | 300 |
| 20 | 98.901 | 9.8901 | 191.2053 | 300 |

### 3.1.3 Manufacturing process

The process of fabricating the MRE begins with mixing the two components of silicone rubber MM228 with ratio of 10:1 and the desired percentage of magnetic particles in

a disposable container around three minutes. The desired percentage of CIP is added first to Part A of silicone rubber and the hardener of Part B silicone rubber is added as the last component, with its corresponding weight are according to Section 5.3. This is because the curing process starts as soon as the hardener is added to other components.

Then the mixture is placed into a vacuum chamber for 10 minutes to remove any trapped air inside the mixture. All surfaces of the mould that will have contact with the mixture were sprayed with silicone release agent for ease of removing the MRE from the mould. Immediately after the degassing process, the MRE mixture was poured into the specific moulds. The moulds are fabricated using aluminium material because it's non-ferromagnetic property and it will not be magnetized when permanent magnets are used to cure anisotropic sample.

Samples for impact hammer test were made in accordance with BS ISO 7743-2011 [68]. Type A cylindrical sample has diameter of 29 mm and height of 12.5 mm. The mould is designed to produce 12 samples for each curing process. For anisotropic samples, neodymium permanent magnets can be utilized and in place whilst the MRE mixture is cured inside the mould. A total of eight square magnets, four at each side of the moulds, can be fix to generate an average of 430 mT magnetic field for fabricating anisotropic samples. However only isotropic samples with the variation as in Table 3.3 are manufactured and tested.

## 3.2 Modal testing

In this work, modal testing method is considered. By comparing to the three methods that mentioned in 2.5.1, which are shear, tensile and compression test, modal testing is a simple measurement approach to characterize MRE property because of less hardware required and it provide faster measurement time. By using hand-held device such as impact hammer and accelerometers, the FRF can be obtained to determine natural frequency and loss factor of the MRE. Two different setups which are zero and with magnetic field, are cogitated. The cylindrical MRE sample is placed in between a steel cylinder with similar diameter and concrete block or layers of permanent magnetic for zero or with magnetic field setup respectively. Figure 3.1 shows impact test setup with magnetic field. An accelerometer is attached to top of the cylindrical steel and on surface of concrete block. The Accelerometer 1 will capture the response of the test setup upon force excitation of the impact hammer. Meanwhile the presence of the Accelerometer 2 is to provide any indication if the base of the test setup is vibrating or stationary during the force excitation. Gauss meter is placed at the middle of MRE height for magnetic field intensity measurement.

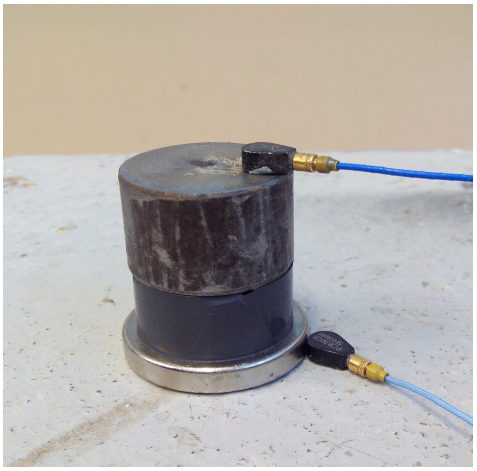

(a) Impact hammer test setup with the presence of permanent magnet.

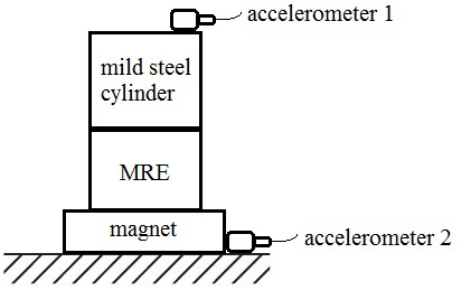


(b) Simplified diagram of Figure 3.3(a)

FIGURE 3.1: Impact hammer test configuration.

For both setup, point force from impact hammer is applied four times to the cylindrical steel mass. MRE with different CIP contents is replaced with variation as in Table 3.3 for different set of measurement. Four MRE samples with similar CIP content that fabricated from the same mixture are utilized in order to get average property of MRE. Then force response from impact hammer, accelerance, coherence and phase will be plotted from data acquisition system. Figure 3.2 and Figure 3.3 depict the average four reponsess from test setup with 5% CIP MRE without permanent magnet and 10% CIP MRE with a layer of permanent magnet from the Accelerometer 1. All measurements used for obtaining MRE property are chosen based on the consistency of force response and coherence plots as shown in both Figure 3.2 and Figure 3.3. For the force response, the only measurement that will be utilized is one with amplitude of the force spectrum is not exceeding 10 dB to 20 dB down at the maximum frequency of interest. Then the next criteria of choosing accurate measurement are to observe the coherence plot where the magnitude must be close to one for the entire frequency range and the consistent close-to-zero response from the Accelerometer 2. If there was a waveform observed right after force impulse applied to the MRE, the base setup need to be adjusted as it indicates a movement.

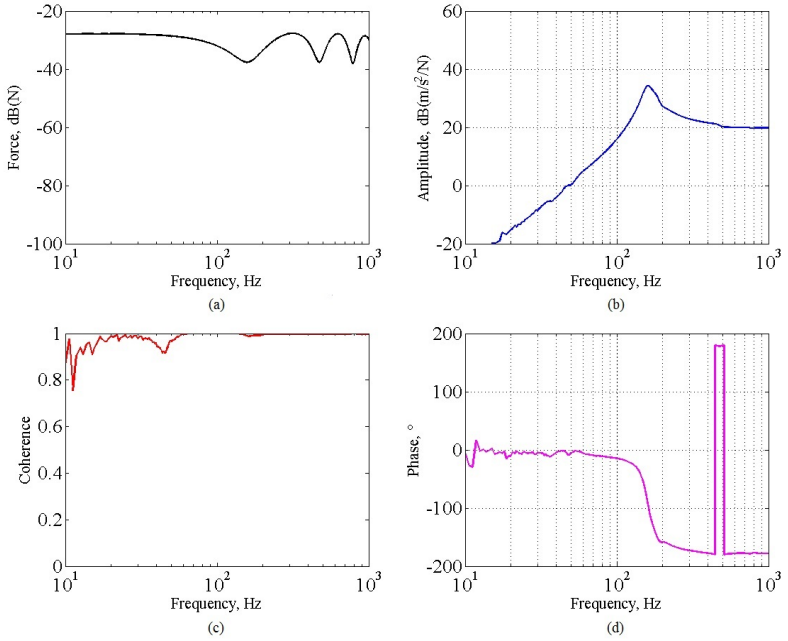


FIGURE 3.2: Measurement of impact hammer test on 10% CIP MRE without magnetic field. (a) force spectrum, (b) accelerance magnitude, (c) coherence and (d) accelerance phase.

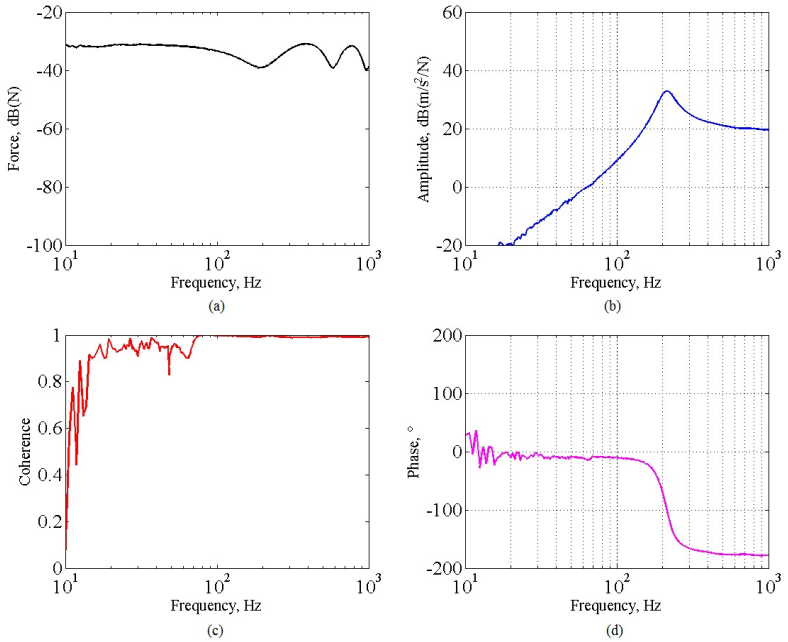


FIGURE 3.3: Measurement of impact hammer test on 20% CIP MRE with magnetic field, 52 mT. (a) force spectrum, (b) accelerance magnitude, (c) coherence and (d) accelerance phase.

In order to define the property of MRE, the test setup is assumed to be a single-degree-of-freedom system and the effective mass is governed by [69]

$$m_{eff} \simeq m_{steel} + \frac{m_{MRE}}{3} \tag{3.2}$$

where $m_{steel}$ and $m_{MRE}$ are the mass of cylindrical steel and MRE sample respectively. Natural frequency of the single-degree-of-freedom system is determined by maximum magnitude of the frequency response. Estimation of MRE sample stiffness $k_{MRE}$ can be accomplished by two approaches. Firstly, by using the known value of natural frequency $\omega_n$ from the maximum accelerance, $k_{MRE}$ can be determined as

$$k_{MRE} = \omega_n^2 m_{eff} \tag{3.3}$$

The other approach is by estimating $k_{MRE}$ from the value of the straight line that constitutes part of accelerance plot starting from low frequency until the maximum accelerance. As shown in Figure 3.4, $k_{MRE}$ can be estimated by

$$A(\omega) \simeq \frac{\omega^2}{k_{MRE}} \tag{3.4}$$

where $A(\omega)$ is the accelerance.

At higher frequency range of accelerance plot, which is after the maximum accelerance, a horizontal line is also useful to verify the $m_{eff}$ of the single-degree-of-freedom.

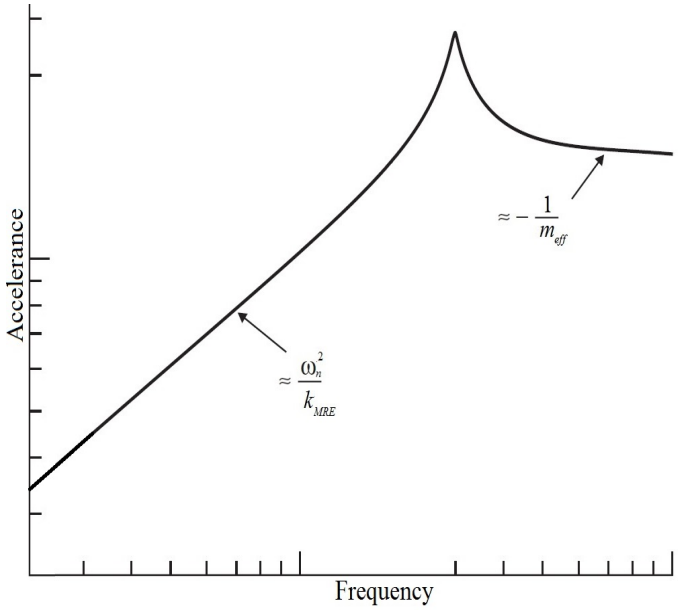


FIGURE 3.4: Magnitude of accelerance FRF plot.

By choosing a partial range of frequency response that start and finish 3 dB or $\sqrt{2}$ down of the maximum point, Nyquist plot will be used to approximate the value of damping property or loss factor. The circle fit technique will try to match a circle to the real and imaginary part of the frequency response. Fitting process is done by minimizing discrepancy between the radius of measured data and the fitted circle. By referring to Figure 3.5, additional two adjacent frequencies, $\omega_a$ and $\omega_b$, that lie on the fitted circle are required for estimating loss factor of MRE sample. The loss factor can be determined by [70]

$$\eta \simeq \frac{2(\omega_a - \omega_b)}{\omega_n\left(\tan\left(\frac{\theta_a}{2}\right) + \tan\left(\frac{\theta_a}{2}\right)\right)} \tag{3.5}$$

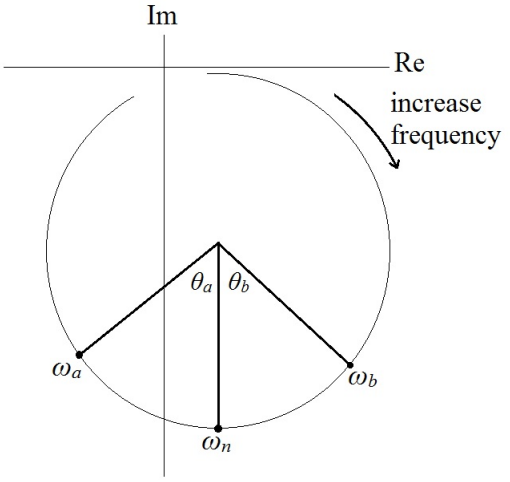


FIGURE 3.5: Nyquist plot for estimating loss factor of MRE sample

### 3.2.1 Results and discussion

From the modal testing and the related equations from Equation 3.2 until 3.5, the result from the impact hammer measurement are presented in Figure 3.6(a) and Figure 3.6(b) for 10% and 20% CIP respectively. The measurement started with a zero-field condition, which is without any permanent magnet. Then the procedure is repeated with a single permanent magnet with a measured field of 52 mT up until four stacks of magnets of 175 mT, as shown in Figure 3.1.

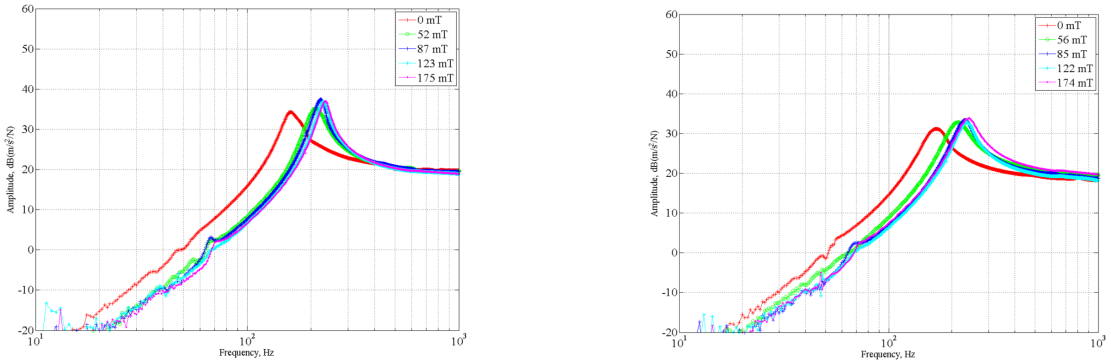


(a) Result of 10% CIP

(b) Result of 20% CIP

FIGURE 3.6: Measured accelerance of MRE modal testing with different applied magnetic field.

For both figures, the peak of each accelerance that signify natural frequency of the measured setup, shows an increasing trend as the applied magnetic field is increased. Due to different content of CIP volume, the value of natural frequency for 20% CIP sample is always higher than corresponding 10% CIP for equivalent setup. MRE stiffness, $k_{MRE}$ is then calculated and estimated by referring to Equation 3.3 and 3.4, of which the latter utilized polyfit function in MATLAB. Both values is compared and details of the measured values is tabulated in Table 3.4.

TABLE 3.4: Impact hammer measurement data and $k_{MRE}$ stiffness estimation from accelerance plot as in Figure 3.6.

| CIP % | Magnetic field, mT | Natural frequency, Hz | Loss factor | Estimated stiffness, $10^5$ N/m | |
|---|---|---|---|---|---|
| | | | | $k_1$ | $k_2$ |
| 10 | 0 | 161.92 | 0.19236 | 1.022 | 1.064 |
| | 52 | 209.95 | 0.18975 | 1.716 | 1.789 |
| | 87 | 220.66 | 0.12533 | 1.895 | 1.976 |
| | 123 | 226.24 | 0.12066 | 1.992 | 2.007 |
| | 175 | 232.05 | 0.11887 | 2.096 | 2.185 |
| 20 | 0 | 173.06 | 0.28119 | 1.167 | 1.226 |
| | 56 | 216.27 | 0.24581 | 1.821 | 1.915 |
| | 85 | 228.62 | 0.18794 | 2.035 | 2.139 |
| | 122 | 238.72 | 0.20069 | 2.218 | 2.333 |
| | 174 | 247.99 | 0.24548 | 2.394 | 2.518 |

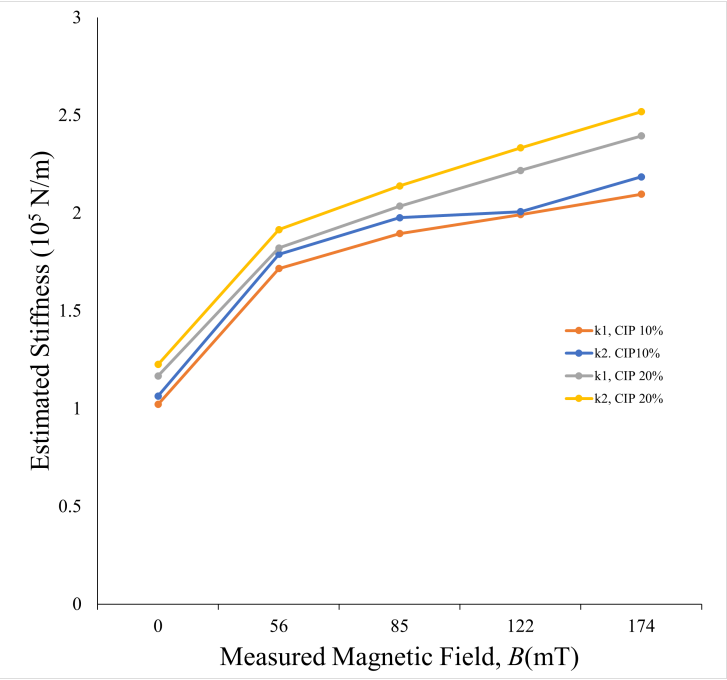


FIGURE 3.7: Estimated stiffness of 10% and 20% against measured magnetic field.

Figure 3.7 depicts the estimated 10% and 20% CIP MRE stiffness with respect to increasing magnetic field. $k_1$ and $k_2$ are the estimated stiffness values that utilize Equation 3.3 and 3.4 repectively. Both equations estimated almost the same value for each measured magnetic field with only around 5% different. Therefore, an average value of $k_{MRE}$ for each magnetic field value is taken from both estimated stffness values. In general, it can be seen that as the MRE stiffness is increased, of which contributed by increasing natural frequency, as the applied magnetic field is increased. 20% CIP MRE has higher stiffness value for every measured magnetic field value and it is consistent with the additional CIP contents compared with 10% CIP MRE. All samples that used in the test having the same dimension and direct relation between $k_{MRE}$ and $E_{MRE}$ can be referred to as in Equation 5.10. These results on increasing $k_{MRE}$, of which directly proportion to $E_{MRE}$, are in a good agreement with most reported literature as mention in Section 2.5.1. An increase in the induced magnetic field will increase magnetic interaction between CIP in MRE. As the interaction force is larger, an equivalent reaction force from the elastic component of MRE will be generated to reach the equilibrium state as mentioned in Section 4.2.1 and correspondingly increase the modulus of MRE.

However, the trend for loss factor is decreasing as the induced magnetic field is increased. It can be seen only for the 10% sample. For the 20% sample, no clear trend can be concluded. By comparing loss factor value in the perspective of CIP content in MRE, the value is improved for each measured magnetic field. This trend is also true for the stiffness value. Therefore, increase in CIP percentage will improve damping capacity and the Young's modulus of which also reported in [29], [30], [31], [33] and [35].

## 3.3 Conclusions

This chapter briefly explained the fabrication of the isotropic MRE sample. Starting from involved material and followed by mixing compound, manufacturing process until the testing procedure of the MRE sample. The type of material and the manufacturing process utilized in this chapter can be considered common aspects of which many researchers already implemented. Sample testing is, however, considering the availability of existing measurement device and faster measurement time, using a modal testing method. Utilization of impact hammer test with consideration of single-degree-of-freedom system, MRE stiffness and lost factor can be determined from accelerance and Nyquist plot respectively. Results from the impact hammer test will be presented and compared with the MRE model in the next chapter including a comparison with existing literature.

# Chapter 4

# MREs Modelling

## 4.1 Introduction

MREs typically comprise of a polymeric matrix with ferromagnetic particles, hence the viscoelasticity and magnetic field interaction properties are the two main components necessary to be included in the modelling of its characteristics. Behavior of MREs characterized using their viscoelastic property has been justified experimentally to explain the dynamic properties when under the influence of magnetic fields [32, 71, 72]. The dynamic shear stiffness of MREs is reported to increase, but changes in the loss factor are positive [32] and uncertain [72] as magnetic fields are applied. Thus it is necessary to model MREs with both zero-field and magnetic-field dependency, so that a clear understanding of the MRE dynamic behaviour can be ascertained.

In this chapter, the quasi-static model of inter-particle reaction of the iron particles in silicone rubber matrix is based on the work by [39]. A new physical-based model approach is assumed by considering compressional stiffness changes by adopting the model derived by [2]. The model will comprise of two parts which are zero field and magnetic dependent component. The first component utilizes the law of mixture to predict Young's modulus of the ferromagnetic and silicone rubber mixture. The latter component that quantifying nonlinear constitutive magnetic field equation is explored and later will be simplified as linearised stiffness around the equilibrium position of the ferromagnetic particle.

## 4.2 Modelling of the magnetic field dependent behaviour of a MRE

The MR effect is commonly known as being that due to the magnetic field induced change of the properties such as dynamic damping and stiffness. Controllability of MRE properties is driven by the fundamental physics of the magnetic interaction between

ferromagnetic fillers inside the MRE. Several assumptions are required in pursuance of such an approach to the modelling of MRE magnetic dependent properties. Filler particles are considered to be homogenous spheres and magnetized to be identical dipoles [1]. At first, two spherical ferromagnetic particles are seperated and distributed by a gap $r_0$ in the elementary cube of silicone rubber matrix with the size $r_0$ as shown by Figure 4.1.

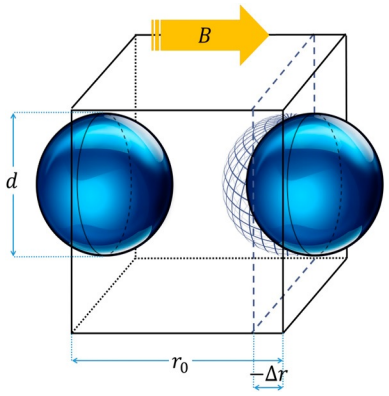


FIGURE 4.1: Two halves of spherical ferromagnetic particle in the elementary cube silicone rubber matrix that seperated by $r_0$ [2]

By considering elimentary cell that represent a cube size $r_0$ including a spherical particle of diameter $d$, the volume fraction of the filler particle in the matrix suspension, $\phi$, is considered as the ratio between the volume of the particle and the volume of the elementary cell

$$\phi = \frac{\pi d^3}{6r_0^3} = \frac{\pi}{6h^3} \tag{4.1}$$

where $h = \frac{r_0}{d}$ is a reciprocal indicator of distance between two particles. For a pure silicone rubber matrix without the particle, the $\phi$ is 0 and $h = \infty$. The maximum $\phi$ can be inferred when $h = 1$, of which the value is $\frac{\pi}{6}$.

A magnetic field is applied parallel to the direction of chains and the particles are evenly distributed in the chains. Before considering to model the MR effect under pure compression, a one-dimensional model of dipole-dipole magnetic interactions under shear is revisited from Jolly et al. [40]. Figure 4.2 depicts the geometry of two adjacent particles within a chain inside the MRE along with the direction of applied magnetic field.

[1] Magnetic dipole is an inherent property of magnet, either in micro or macrostrucuture level, that has magnetic fields connecting the north and the south pole

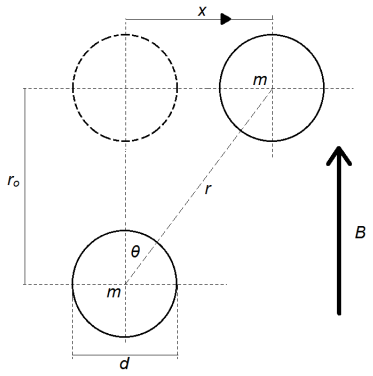


FIGURE 4.2: Geometry of two particles of dipole moments $m$ under shear deformation.

The interaction energy between two dipoles with equal moment [2]. $M$ is given by [73]

$$E = \frac{M^2(1 - 3\cos^2\theta)}{4\pi\mu_0\mu_1 r^3} \tag{4.2}$$

where $\mu_0$ and $\mu_1$ are space and MREs permeability. $r$ is the distance between two adjacent dipoles and it can be expressed in term of horizontal component, $x$ and vertical component $r_0$ as $r = (x^2 + r_0^2)^{\frac{1}{2}}$. From Figure 4.2, by applying trigonometric identities, the angle $\theta$ can be expressed as $\cos\theta = \frac{r_0^2}{(x^2+r_0^2)}$. Scalar strain of the dipoles can be defined as $\varepsilon = \frac{\triangle r}{r_0}$. Thus, Equation (4.2) can be rewritten as

$$E = \frac{M^2(\epsilon^2 - 2)}{4\pi\mu_0\mu_1(\varepsilon^2 + 1)^{\frac{5}{2}} r_0^3} \tag{4.3}$$

The interaction energy between dipoles per unit volume, energy density $U$ can be obtained by dividing Equation (4.3) with the total volume of the elementary cell, $r_0^3 = \frac{\pi d^3}{6\phi}$

$$U = \frac{3M^2(\varepsilon^2 - 2)}{2\pi\mu_0\mu_1 r_0^3 d^3(\varepsilon^2 + 1)^{\frac{5}{2}}} \tag{4.4}$$

where $d$ is diameter of the particle and $\phi$ is the volume fraction of particles inside the MRE. The stress induced by an applied magnetic field through the particle can be calculated by differentiating Equation (4.4) with respect to the scalar strain as

$$\sigma = \frac{\partial U}{\partial \varepsilon} = \frac{9M^2\phi\varepsilon(4 - \varepsilon^2)}{2\pi^2\mu_0\mu_1 r_0^3 d^3(\varepsilon^2 + 1)^{\frac{7}{2}}} \tag{4.5}$$

By considering average particle polarization $J_p$, which accounts dipole moment magnitude $M$ per unit volume as

$$M = J_p V = \frac{J_p \pi d^3}{6} \tag{4.6}$$

[2]Magnetic dipole moment is a torque (vector quantity) that experienced by a magnetic dipole under the influence of applied magnetic field.

the shear modulus $G$ of a MRE is given by

$$G = \frac{J_p^2 \phi \varepsilon (4 - \varepsilon^2)}{8h^3 \mu_0 \mu_1 (1 + \varepsilon^2)^{\frac{7}{2}}} \tag{4.7}$$

A similar approach has been taken for an MRE under pure compression and two adjacent particles geometry under that condition is shown in Figure 4.3. From Figure 4.3, distance between dipoles is now $r = r_0(1 + \varepsilon)$ and the angle $\theta$ is zero, thus $\cos\theta = 1$.

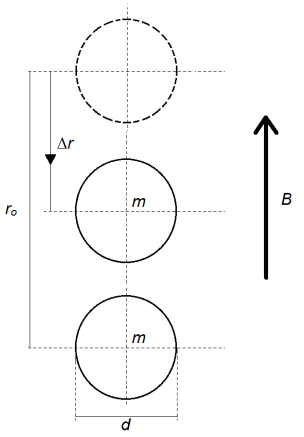


FIGURE 4.3: Geometry of two adjacent particles in a longitudinal chain along with the applied magnetic field $B$ parallel to the particle chain.

So Equation (4.2) can be rewritten as the interaction energy between the two particles are given by

$$E = -\frac{M^2}{2\pi \mu_0 \mu_1 (1 + \varepsilon)^3 r_0^3} \tag{4.8}$$

By repeating the same steps from Equation (4.4), energy density of dipoles $U$ can be rewritten as

$$U = -\frac{3M^2 \phi}{\pi^2 \mu_0 \mu_1 (1 + \varepsilon)^3 r_0^3 d^3} \tag{4.9}$$

Then, the stress induced by the applied magnetic field can be obtained by differentiating Eq .(4.9) with respect to the scalar strain as

$$\sigma = \frac{\partial U}{\partial \varepsilon} = \frac{9M^2 \phi}{\pi^2 \mu_0 \mu_1 (1 + \varepsilon)^4 r_0^3 d^3} \tag{4.10}$$

By repeating the same steps from Equation (4.6) and substituting $h$ from Equation (4.1), the nonlinear induced stress can be expressed as

$$\sigma = \frac{3J_p^2\phi^2}{2\pi^2\mu_0\mu_1(1+\varepsilon)^4} \tag{4.11}$$

Equations (4.7) and (4.11) are in term of average particle polarization $J_p$. Jolly et al. [40] stated that average particle polarization $J_p$ is difficult to compute and measure directly, which is unlike the applied magnetic field $B$ that can be obtained and measure directly using a flux meter. Thus, Jolly et al. [40] developed a relationship between the average particle polarization $J_p$ and the applied magnetic field $B$ by considering particle saturation model. The model is established on the basis of magnetic saturation of particle starts at minimum level of applied magnetic field and reaches maximum particle saturation as level of applied magnetic field increased. The relationship of $Jp$, $B$ and $\alpha$ are given by [40] as

$$J_p = \frac{1.5\alpha^3 B + (1-\alpha^3)J_s}{1+1.5\phi\alpha^3} \tag{4.12}$$

$$\alpha = \frac{3 - \frac{2}{\phi} + \sqrt{(3-\frac{2}{\phi})^2 + 12k(\frac{2}{\phi}(1-k\frac{B}{B_s}) + 3(k-1))}}{6k} \tag{4.13}$$

$J_s$ and $B_s = J_s + \mu_0 H$ are the saturation of polarization and saturation flux density respectively. $H$ is measurable field strength, which is governed by $B = \mu_0 H$. $k \geq 1$ is a parameter that used to satisfy magnetic interaction between adjacent particle chains and complex chain structures [40, 54]. Parameter $k$ is also used and adjusted to fit the model to experimental data. By substituting Equation (4.12) into Equation (4.7) and (4.11), field-dependency modulus of MRE under shear and pure compression can be obtained respectively.

### 4.2.1 Linearised MRE modulus

In this section, the derivation of the linearised MRE modulus is based on the work done by [2]. The basic idea of linearising the modulus is when an external magnetic field is applied to MRE, it will caused CIP attraction inside the matrix. It is also can be anticipated as an external force acting and subsequently compressing the MRE. Thus, at the same time, the elasticity of MRE will oppose such external force until an equilibrium state is reached. During the equilibrium state, a small displacement can be considered to estimate combined linearised modulus. Initially, modulus of MRE without the influence of the magnetic field, $E_{mag0}$, is defined by

$$E_{mag0} = \frac{E_{CIP}E_{SR}}{(1-\phi)E_{CIP} + \phi E_{SR}} \tag{4.14}$$

$E_{mag0}$ is based on the series model between $E_{CIP}$ and $E_{SR}$. From Figure 4.4, a comparison is made between series model, parallel model, and data measured as per Section 3.3. The data from Section 3.3 that utilized in this comparison were calculated by taking average value of estimated $k1$ and $k2$ of 10% and 20% MRE at 0 mT. Then the stiffness value is converted to equivalent $E_{mag0}$ that based on Equation 5.10. The series model can provide a better approximation of macroscopic modulus of elasticity and in quite good agreement with the same order of magnitude predicted by the experimental data.

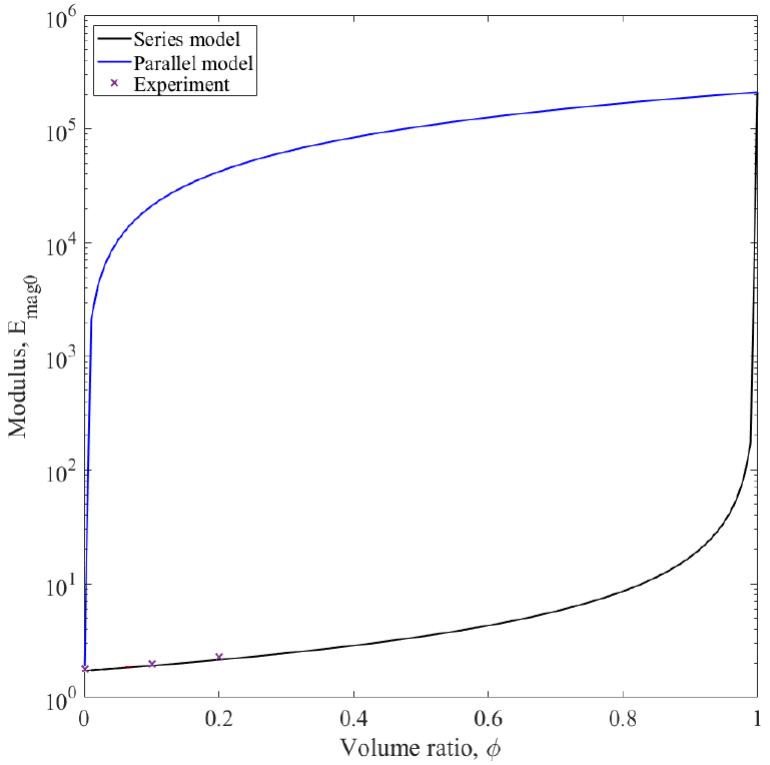


FIGURE 4.4: A comparison of series model, parallel model, and experimental results of $E_{mag0}$ with the variation of CIP volume ratio, $\phi$.

Then, by considering stresses at the equilibrium state between nonlinear magnetic stress of Equation (4.11) and Equation (4.14) times with scalar strain $\varepsilon$, the relation can be written as

$$\frac{3J_p^2\phi^2}{2\pi\mu_0\mu_1(1+\varepsilon)^4} = -E_{mag0}\varepsilon \tag{4.15}$$

The static equilibrium strain can be solved from fifth order polynomial by rearranging Equation (4.15) as

$$\varepsilon^5 + 4\varepsilon^4 + 6\varepsilon^3 + 4\varepsilon^2 + \varepsilon + C = 0 \tag{4.16}$$

where

$$C = \frac{3J_p^2\phi^2}{2\pi\mu_0\mu_1 E_{mag0}} \tag{4.17}$$

Only one root of the polynomial will be then used to determine the static equilibrium position. The root is chosen based on its value that fall within the range of $-1 \leq \varepsilon \leq 0$. The relation between $\sigma$ and $\varepsilon$ can be linearly approximated within small strain range around the equilibrium position, $\varepsilon_{eq}$ using Taylor's series expansion. The term $(1+\varepsilon)^4$ in the denominator of Equation (4.11) can be expanded as

$$(1+\varepsilon)^{-4} \approx (1+\varepsilon_{eq})^{-4} - 4(1+\varepsilon)^{-5} \triangle \varepsilon \tag{4.18}$$

where $\varepsilon_{eq} = \varepsilon - \triangle\varepsilon$ is the equilibrium strain that accounts further MRE deformation, $\triangle\varepsilon$ after the static equilibrium state is achieved. Therefore, the linearised magnetic Young's modulus can be expressed as

$$E_{mag} = \frac{6J_p^2\phi^2}{\pi\mu_0\mu_1(1+\varepsilon_{eq})^5} \tag{4.19}$$

Hence, the total linearised MRE modulus, $E_{MRE}$ that account zero-field and induced magnetic field properties can be written as

$$E_{MRE} = E_{mag0} + E_{mag} \tag{4.20}$$

## 4.3 Results

In this section, the linearised MRE modulus model in Equation (4.20) will be verified with existing literature and the result is shown in Table 4.1. The table outlines the data sourced from [3] and [4]. Then, the simulated curves of the linearised model were plotted against increasing induced magnetic field. It is adequate to mention that selection of $k$ parameter, of which in Equation (4.13), is merely on interpolating approach. A basic guideline was however, provided by [40] that the $k \geq 1$. The challenge is to predict a baseline value for different MRE matrix and CIP composition especially for zero-field modulus. Once the predicted modulus with known $k$ value, matches with measured data, the model can predict the magnetic dependent property or MR effect fairly accurate. Both sources have reported the static compression test. Hence, the experimental data from those sources were ideal for comparison purpose with the developed linearised MRE modulus model.

TABLE 4.1: Compression model of linearised MRE modulus: data comparison with [3], [4] and modal testing experiment.

| Data Source | CIP % | MRE Type | MRE modulus, $E_{MRE}$ (MPa) | | | Error % | $k$ |
|---|---|---|---|---|---|---|---|
| | | | Zero field | Magnetic Field | Linearised Model | | |
| Schubert 2014 | 10 | Isotropic | 0.95 | 1.0788 (210 mT)<br>1.1373 (450 mT) | 1.0215<br>1.1337 | 5.31<br>0.32 | 4.7 |
| | 20 | Isotropic | 1.25 | 1.5051 (210 mT)<br>1.8205 (450 mT) | 1.4289<br>1.8147 | 5.06<br>0.32 | 10 |
| | 30 | Isotropic | 1.75 | 2.4288 (210 mT)<br>3.1610 (450 mT) | 2.1506<br>3.1578 | 11.45<br>0.01 | 20 |
| Kallio 2005 | 30 | Ansotropic | 1.9818 | 2.3256 (180 mT)<br>2.7917 (350 mT)<br>3.4167 (680 mT)<br>3.75 (1 T) | 2.1295<br>2.4448<br>3.1807<br>3.764 | 8.43<br>12.43<br>6.91<br>0.37 | 14 |
| Modal test | 10 | Isotropic | 1.9736 | 3.3165 (52 mT)<br>3.6628 (87 mT)<br>3.784 (123 mT)<br>4.051 (175 mT) | 3.624<br>4.0479<br>4.4151<br>4.6362 | 9.27<br>10.51<br>16.67<br>14.45 | 6.7 |
| | 20 | Isotropic | 2.264 | 3.5351 (56 mT)<br>3.9495 (85 mT)<br>4.3063 (122 mT)<br>4.6479 (174 mT) | 3.4651<br>4.0834<br>4.5128<br>4.606 | 1.98<br>3.39<br>4.8<br>0.9 | 13 |

For Figure 4.5 (a), (b), and (c), only three data of the isotropic MRE at the corresponding magnetic field were extracted from [3] due to utilization of a limited permanent magnet that utilized in reported experimental works. As for anisotropic MRE reported in [4], the static compression testing was performed with the presence of electromagnet. Only five recorded magnetic field values were reported in the test and the values were directly estimated from measured stress-strain curves. Overall, the developed linearised MRE modulus model can fairly estimate the experimental data from [3] and [4].

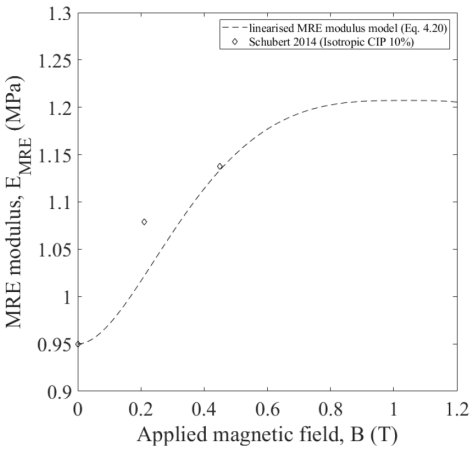


(a) Linearised modulus model vs CIP 10% [3]

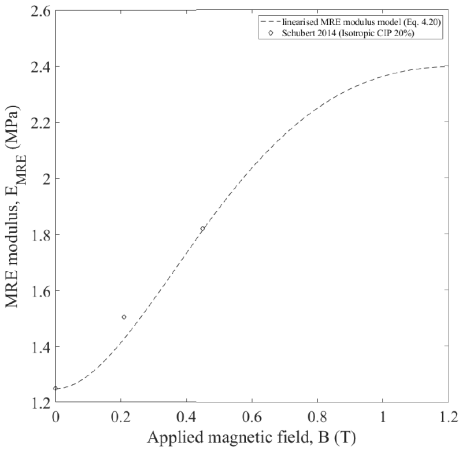


(b) Linearised modulus model vs CIP 20% [3]

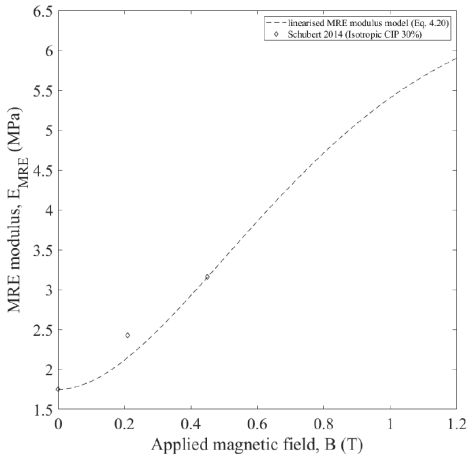


(c) Linearised modulus model vs CIP 30% [3]

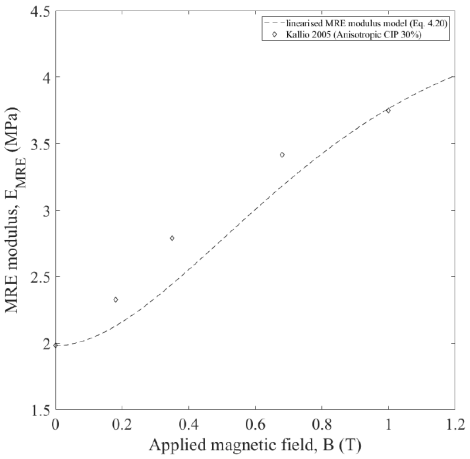


(d) Linearised modulus model vs CIP 30% [4]

FIGURE 4.5: Comparison of simulated curve of linearised MRE modulus model, $E_{MRE}$ with (a) 10% isotropic MRE by [3] (b) 20% isotropic MRE by [3](c) 30% isotropic MRE by [3] (d) 30% anisotropic MRE by [4].

## 4.4 Conclusion

As a conclusion for this section, the linearised modulus MRE model, $E_{MRE}$, comprises two components that are zero-field, $E_{mag0}$ and magnetic dependent property, $E_{mag}$. The zero-field property is defined by the series configuration of silicone rubber and CIP modulus and its corresponding volume percentage. The selection criteria of such configuration are due to the adequacy of the law of mixture that fits reasonably good with experimental finding. Meanwhile, magnetic-field dependency properties of MRE under the compression is modelled by altering the shear model of dipole-dipole particle interaction introduced by [40]. By considering small strain changes around an equilibrium state, the magnetic dependent modulus is linearly approximated by utilizing Taylor's series expansion of fifth order. Due to such approximation, this model is limited to linear

elastic response and will not suitable for hardening of the MRE when a large magnetic field is induced. However, the linearised model, which can predict fairly accurate two sources of data from existing literature and experimental results from modal testing, can be beneficial for estimating MRE stiffness or modulus for different CIP concentration under the influence of the magnetic field. Theoretical estimation of the lower and upper range of MRE modulus can provide beneficial gain in switchable stiffness application.

# Chapter 5

# Mathematical Modelling of Rotor-Bearing System

## 5.1 Introduction

In this chapter, a mathematical model of a rotor-bearing system supported on flexible mounts is developed. From the previous chapter, the linearised MRE modulus equation will be incorporated in the mounting model. Generally, rotating machinery is known to encounter lateral vibration during its range of operating service. The imbalance of an uneven mass distribution of the rotor, instability of the supporting device or structure of the shaft and other potential external forces acting on the system can result in a serious malfunction of the rotor-bearing system. As the operational speed varies, the critical speed and natural frequency of the system will alter accordingly and affect the performance of the system.

A simplified lumped parameter model of a rotor-bearing system is a popular model used to analyze the dynamics of a single rotor supported on bearings. Bearings can take many forms, which depend upon specific assumptions, such as simple bushing, rolling-element and a wide range of journal types. These bearings are normally assumed to be attached on a fixed support, so that performance of the bearings can be evaluated specifically for the whole system dynamics.

Thus, in this chapter the dynamics of a simple rotor-bearing system on flexible supports will be examined. As the system is supported on two bearings at the two ends of a shaft, it is assumed that the bearings will be mounted on flexible material. The main focus is to implement viscoelastic material into the system. In parallel with the advancement of modelling viscoelastic material [1, 17–22], which help to describe the complexity of the material properties, the application of viscoelastic components in rotordynamics has generally increased as well. Effects on the threshold speed, natural frequency and the

temperature sensitive behaviour on the dynamic characteristics have been discussed in [23, 24]and [5] respectively as viscoleastic support properties vary. Furthermore, viscoelastic supports in rotor-bearings systems are reported to be beneficial in attenuating noise and vibration [25, 26].

## 5.2 Mathematical Model

In this section, the mathematical modelling of a rigid rotor supported on flexible supports is demonstrated. Generally, the equations of motion of a rigid rotor mounted on flexible supports are derived where the latter are comprised of elastic or viscoelastic supports. The flexible support model is assumed to have a linear spring and viscous damping in parallel, while the viscoelastic support model is based on the standard linear model. For both type of supports, the rotor-bearing system is assumed to consist of a rigid rotor, a massless and rigid shaft supported on two identical short bearings, and the bearings are flexibly supported in both the horizontal and vertical directions.

A right-handed coordinate system is utilized to define the motion of the rotor-bearing system as shown by Figure 5.1. The rigid rotor of mass $m$, spins around the $Z$-axis with angular velocity $\Omega$ and moves horizontally and vertically in the $X$ and $Y$ axes respectively. Gyroscopic couples act on the system by definition of angular momentum conservation that are perpendicular to the axis of spin. The direction of the moments about the $X$ and $Y$ axes are specified by angular direction of $\psi$ and $\theta$ shown in Figure 5.1 respectively.

### 5.2.1 Viscously damped supports

From first principles, the equations of motion for the rigid rotor supported by viscously damped flexible supports including unbalance and external moments are

$$\begin{aligned} m\ddot{x} + c_{xT}\dot{x} + c_{xC}\dot{\psi} + k_{xT}x + k_{xC}\psi &= m\epsilon\Omega^2\cos(\Omega t + \delta) \\ m\ddot{y} + c_{yT}\dot{y} - c_{yC}\dot{\theta} + k_{yT}y - k_{yC}\theta &= m\epsilon\Omega^2\sin(\Omega t + \delta) \\ I_d\ddot{\psi} - I_p\Omega\dot{\theta} + c_{xC}\dot{x} + c_{xR}\dot{\psi} + k_{xC}x + k_{xR}\psi &= (I_d - I_p)\beta\Omega^2\cos(\Omega t + \gamma) \\ I_d\ddot{\theta} + I_p\Omega\dot{\psi} - c_{yC}\dot{y} + c_{yR}\dot{\theta} - k_{yC}y + k_{yR}\theta &= (I_p - I_d)\beta\Omega^2\sin(\Omega t + \gamma) \end{aligned} \tag{5.1}$$

where $I_d$ and $I_p$ are the diametral and polar moment of inertia of the rotor respectively. $\epsilon$ and $\beta$ are the rotor eccentricity and skewed centerline angle respectively. $\delta$ and $\gamma$ are the initial condition values of each horizontal, vertical and two angular displacements of the rotor.

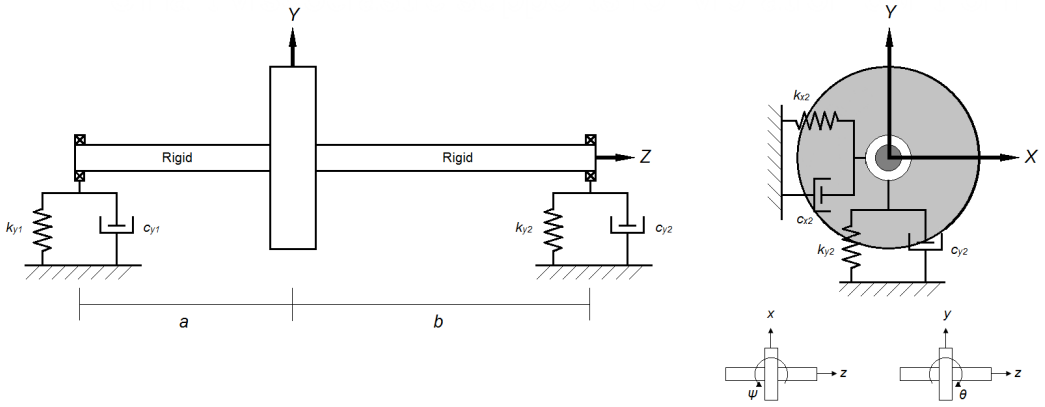


FIGURE 5.1: A rigid axisymmetric rotor on viscously damped supports and with definition of the coordinate system $X$, $Y$, and $Z$, origin at the static centre of mass of the rotor.

Stiffness and damping coefficients in Equation (5.1) are expressed in term of a combination of each element from the two bearings by

$$\begin{aligned} S_{iT} &= S_{i1} + S_{i2} \\ S_{iC} &= -aS_{i1} + bS_{i2} \\ S_{iR} &= a^2 S_{i1} + b^2 S_{i2} \end{aligned} \tag{5.2}$$

where $S$ are $k$ or $c$ for stiffness or damping coefficients respectively, and $i$ is either $x$ or $y$. The subscript $T$, $C$ and $R$ are used to describe the translational coefficient ($T$), coupling coefficient between translational and rotation ($C$) and rotational coefficient ($R$).

For free vibration analysis, all right hand terms in Equation (5.1) are set to be 0. For convenience it can be converted to a state-space equation in the form of

$$\mathbf{A}\dot{\mathbf{x}} + \mathbf{B}\mathbf{x} = \mathbf{0} \tag{5.3}$$

where the arrangement of Equation (5.1), as in Equation (5.3) can be written as

$$\begin{bmatrix} \mathbf{C} & \mathbf{M} \\ \mathbf{M} & \mathbf{0} \end{bmatrix} \frac{\mathrm{d}}{\mathrm{d}t} \begin{Bmatrix} \mathbf{q} \\ \dot{\mathbf{q}} \end{Bmatrix} + \begin{bmatrix} \mathbf{K} & \mathbf{0} \\ \mathbf{0} & -\mathbf{M} \end{bmatrix} \begin{Bmatrix} \mathbf{q} \\ \dot{\mathbf{q}} \end{Bmatrix} = \begin{Bmatrix} \mathbf{0} \\ \mathbf{0} \end{Bmatrix} \tag{5.4}$$

where

$$\mathbf{A} = \begin{bmatrix} \mathbf{C} & \mathbf{M} \\ \mathbf{M} & \mathbf{0} \end{bmatrix}, \mathbf{B} = \begin{bmatrix} \mathbf{K} & \mathbf{0} \\ \mathbf{0} & -\mathbf{M} \end{bmatrix}, \dot{\mathbf{x}} = \frac{\mathrm{d}}{\mathrm{d}t} \begin{Bmatrix} \mathbf{q} \\ \dot{\mathbf{q}} \end{Bmatrix}, \mathbf{x} = \begin{Bmatrix} \mathbf{q} \\ \dot{\mathbf{q}} \end{Bmatrix} \tag{5.5}$$

The corresponding mass $\mathbf{M}$, damping and gyroscopic $\mathbf{C}$, and stiffness $\mathbf{K}$ matrices are

$$\mathbf{M} = \begin{bmatrix} m & 0 & 0 & 0 \\ 0 & m & 0 & 0 \\ 0 & 0 & I_d & 0 \\ 0 & 0 & 0 & I_d \end{bmatrix}, \mathbf{C} = \begin{bmatrix} c_{xT} & 0 & c_{xC} & 0 \\ 0 & c_{yT} & 0 & -c_{yC} \\ c_{xC} & 0 & c_{xR} & -I_p\Omega \\ 0 & -c_{yC} & I_p\Omega & c_{yR} \end{bmatrix}, \mathbf{K} = \begin{bmatrix} k_{xT} & 0 & k_{xC} & 0 \\ 0 & k_{yT} & 0 & -k_{yC} \\ k_{xC} & 0 & k_{xR} & 0 \\ 0 & -k_{yC} & 0 & k_{yR} \end{bmatrix} \tag{5.6}$$

and the degrees of freedom are represented as

$$\mathbf{q} = \begin{Bmatrix} x & y & \psi & \theta \end{Bmatrix}^T \tag{5.7}$$

The state-space matrix of Equation (5.4) can be solved numerically for a single value rotor speed $\Omega$ and the respective complex eigenvalues $s_n$ will represent the damping ratio $\zeta$ and damped natural frequency $\omega_d$, which are in the form

$$\begin{aligned} s_n &= -\zeta_n + i\omega_{dn} \\ s_{n+4} &= -\zeta_n - i\omega_{dn} \end{aligned} \tag{5.8}$$

where $n$ is 1,2, 3, or 4. The relationship between the damped natural frequency $\omega_{dn}$ and natural frequency of the particular system $\omega_n$ is assumed to be given, as for the single degree of freedom viscously damped system [74], by

$$\omega_{dn} = \omega_n\sqrt{1-\zeta_n^2} \tag{5.9}$$

Since the motion of the rotor is defined in four degrees of freedom, so the roots of $s_n$ and $s_{n+4}$ form a complex conjugate pair for each $n$.

### 5.2.2 Smart Viscoelastic supports

For viscoelastic materials, the viscously damped flexible supports in Figure 5.1 are replaced by the standard linear model viscoelastic supports that comprise an internal variable approach to incorporate the frequency dependence of the support modulus, as depicted in Figure 5.2. The supports are also make use of linearised MRE modulus model as in Equation (4.20) and converted to equivalent linearised MRE stiffness, $k_{MRE}$ based on principle of vertical stiffness of rubber [75], as

$$k_{MRE} = \frac{E_{MRE}A}{l} \tag{5.10}$$

where $A$ and $l$ are cross-sectional area and length of MRE sample that manufactured as in Section 3.1.3.

Referring to Figure 5.2, $k_\infty$ is the stiffness constant, $\alpha$ and $\tau$ are viscoelastic material properties that can be obtained normally from material testing procedure [76]. Curve

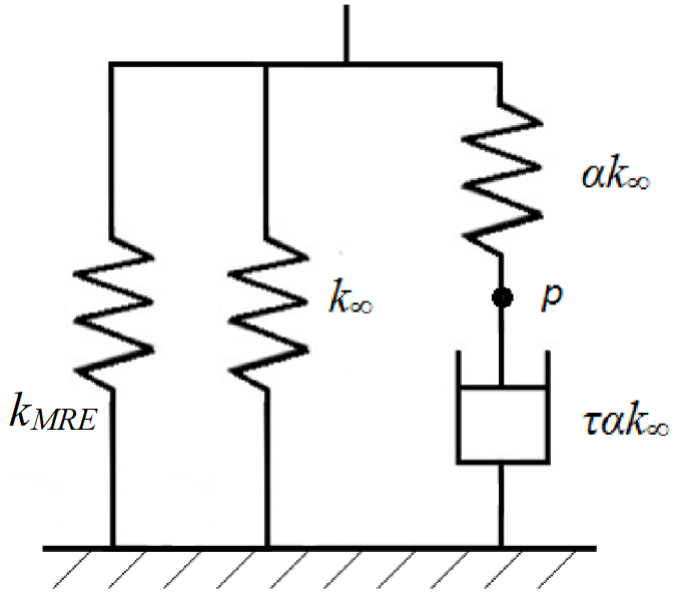


FIGURE 5.2: Standard linear model of flexible support: linearised MRE stiffness, $k_B$ and viscoelastic component.

fitting of the data provides the $\tau$ and $\alpha$ coefficients which are used to determine the complex moduli behaviour of the viscoelastic component. Temporarily in this work, temperature dependency property of viscoelastic is not considered. It will be available for the later stages as temperature variance is considered by having a specific function together with the $\tau$ and $\alpha$ coefficients. From Figure 5.2, forces exerted on the bearings by the viscoelastic supports are derived from first principle, which consider a single internal variable or degree of freedom $p$, at each support for both the $x$ and $y$ directions. The derivation of the forces can be referred to Appendix A.

$$\begin{aligned} f_{x1} &= (k_{MRE} + k_\infty(1+\alpha))(x - a\psi) - k_\infty \alpha p_{x1} \\ f_{y1} &= (k_{MRE} + k_\infty(1+\alpha))(y + a\theta) - k_\infty \alpha p_{y1} \\ f_{x2} &= (k_{MRE} + k_\infty(1+\alpha))(x + b\psi) - k_\infty \alpha p_{x2} \\ f_{y2} &= (k_{MRE} + k_\infty(1+\alpha))(y - b\theta) - k_\infty \alpha p_{y2} \end{aligned} \tag{5.11}$$

By substituting Equation (5.11) into Equation (5.1), the equations of motion for a rigid rotor mounted on identical viscoelastic supports are rearranged as

$$
\begin{aligned}
\ddot{x} &= -\frac{2\hat{k}}{m}x + \frac{\hat{k}(a-b)}{m}\psi + \frac{\hat{a}}{m}(p_{x1}+p_{x2}) + \epsilon\Omega^2\cos(\Omega t+\delta)\\
\ddot{y} &= -\frac{2\hat{k}}{m}y - \frac{\hat{k}(a-b)}{m}\theta + \frac{\hat{a}}{m}(p_{y1}+p_{y2}) + \epsilon\Omega^2\sin(\Omega t+\delta)\\
\ddot{\psi} &= \frac{I_p\Omega}{I_d}\dot{\theta} + \frac{\hat{k}(a-b)}{I_d}x - \frac{\hat{k}(a^2+b^2)}{I_d}\psi - \frac{\hat{a}a}{I_d}p_{x1} + \frac{\hat{a}b}{I_d}p_{x2} + \left(1-\frac{I_p}{I_d}\right)\beta\Omega^2\cos(\Omega t+\gamma)\\
\ddot{\theta} &= -\frac{I_p\Omega}{I_d}\dot{\psi} - \frac{\hat{k}(a-b)}{I_d}y - \frac{\hat{k}(a^2+b^2)}{I_d}\theta + \frac{\hat{a}a}{I_d}p_{y1} - \frac{\hat{a}b}{I_d}p_{y2} - \left(1-\frac{I_p}{I_d}\right)\beta\Omega^2\sin(\Omega t+\gamma)
\end{aligned}
\tag{5.12}
$$

where $\hat{k} = k_\infty(1+\alpha) + k_{MRE}$ and $\hat{a} = k_\infty\alpha$. The example of the derivation of Equation 5.12 can be found in Appendix B. By introducing the additional degrees of freedom, the equations of motion that describe the velocity displacement relationship of the internal variables [76] can be written as

$$
\begin{aligned}
\dot{p}_{x1} &= \frac{1}{\tau}(x - a\psi - p_{x1})\\
\dot{p}_{y1} &= \frac{1}{\tau}(y + a\theta - p_{y1})\\
\dot{p}_{x2} &= \frac{1}{\tau}(x + b\psi - p_{x2})\\
\dot{p}_{y2} &= \frac{1}{\tau}(y - b\theta - p_{y2})
\end{aligned}
\tag{5.13}
$$

The resulting equations of motion in Eqs. (5.12) and (5.13) can be written in a new state space equation [74] as

$$
\dot{\mathbf{r}} = \mathbf{D}\mathbf{r} + \mathbf{w}(t) \tag{5.14}
$$

where

$$
\mathbf{r} = \begin{Bmatrix} \dot{\mathbf{q}} \\ \mathbf{q} \\ \mathbf{u} \end{Bmatrix} \tag{5.15}
$$

with

$$
\mathbf{u} = \begin{Bmatrix} p_{x1} & p_{y1} & p_{x2} & p_{y2} \end{Bmatrix}^T \tag{5.16}
$$

and

$$
\mathbf{D} = \begin{bmatrix} \bar{\mathbf{G}} & \bar{\mathbf{K}} & \bar{\mathbf{V}} \\ I & \mathbf{0} & \mathbf{0} \\ \mathbf{0} & \bar{\mathbf{T}} & \bar{\mathbf{H}} \end{bmatrix} \tag{5.17}
$$

Each element of $\mathbf{D}$ is a $4 \times 4$ matrix where

$$\bar{\mathbf{G}} = \begin{bmatrix} 0 & 0 & 0 & 0 \\ 0 & 0 & 0 & 0 \\ 0 & 0 & 0 & \frac{I_p\Omega}{I_d} \\ 0 & 0 & -\frac{I_p\Omega}{I_d} & 0 \end{bmatrix}, \bar{\mathbf{K}} = \begin{bmatrix} -\frac{2\hat{k}}{m} & 0 & \frac{\hat{k}(a-b)}{m} & 0 \\ 0 & -\frac{2\hat{k}}{m} & 0 & -\frac{\hat{k}(a-b)}{m} \\ \frac{\hat{k}(a-b)}{I_d} & 0 & -\frac{\hat{k}(a^2+b^2)}{I_d} & 0 \\ 0 & -\frac{\hat{k}(a-b)}{I_d} & 0 & -\frac{\hat{k}(a^2+b^2)}{I_d} \end{bmatrix},$$

$$\bar{\mathbf{V}} = \begin{bmatrix} \frac{\hat{a}}{m} & 0 & \frac{\hat{a}}{m} & 0 \\ 0 & \frac{\hat{a}}{m} & 0 & \frac{\hat{a}}{m} \\ -\frac{\hat{a}a}{I_d} & 0 & \frac{\hat{a}b}{I_d} & 0 \\ 0 & \frac{\hat{a}a}{I_d} & 0 & -\frac{\hat{a}b}{I_d} \end{bmatrix}, \bar{\mathbf{T}} = \begin{bmatrix} \frac{1}{\tau} & 0 & -\frac{a}{\tau} & 0 \\ 0 & \frac{1}{\tau} & 0 & \frac{a}{\tau} \\ \frac{1}{\tau} & 0 & \frac{b}{\tau} & 0 \\ 0 & \frac{1}{\tau} & 0 & -\frac{b}{\tau} \end{bmatrix},$$

$$\bar{\mathbf{H}} = \begin{bmatrix} -\frac{1}{\tau} & 0 & 0 & 0 \\ 0 & -\frac{1}{\tau} & 0 & 0 \\ 0 & 0 & -\frac{1}{\tau} & 0 \\ 0 & 0 & 0 & -\frac{1}{\tau} \end{bmatrix}$$

For the forced vibration case, $w(t)$,due to mass unbalance,

$$\mathbf{w}(t) = \begin{bmatrix} \epsilon\Omega^2 \cos(\Omega t + \delta) \\ \epsilon\Omega^2 \sin(\Omega t + \delta) \\ \left(1 - \frac{I_p}{I_d}\right)\beta\Omega^2 \cos(\Omega t + \gamma) \\ -\left(1 - \frac{I_p}{I_d}\right)\beta\Omega^2 \sin(\Omega t + \gamma) \end{bmatrix}$$

$\mathbf{w}(t)$ can be set to zero for the free vibration case and then a standard eigenvalue problem has to be solved. Because of the additional degrees of freedom introduced from the internal variables as in Equation (5.15), the complex conjugate eigenvalues of $S_n$ of Equation (5.8) are now expanded to six pairs instead of four.

## 5.3 Numerical simulations

In this section, several examples will be shown for the free vibration of a rigid rotor mounted on flexible, viscously damped and viscoelastic supports. Subsequently the forced vibration analysis will be presented for specifically a rotor-bearing system supported on identical viscoelastic supports at both ends. In general, the state space matrix

TABLE 5.1: Type of rigid rotor supports and its corresponding parameters for free vibration analysis. The uncoupled system corresponds to symmetric geometry of the rotor and shaft with equal supports at both ends

| **Type of Flexible Support** | **Uncoupled system** | **Coupled system** |
|---|---|---|
| Undamped | $k_{x1} = 1.0$ MN/m<br>$k_{y1} = 1.5$ MN/m<br>$k_{x2} = 1.0$ MN/m<br>$k_{y2} = 1.5$ MN/m | $k_{x1} = 1.0$ MN/m<br>$k_{y1} = 1.5$ MN/m<br>$k_{x2} = 1.3$ MN/m<br>$k_{y2} = 2.0$ MN/m |
| Viscously damped | $k_{x1} = k_{y1} = 1.0$ MN/m<br>$k_{x2} = k_{y2} = 1.0$ MN/m<br>$c_{x1} = c_{x2} = 1.0$ kNs/m<br>$c_{y1} = c_{y2} = 1.2$ kNs/m | $k_{x1} = k_{y1} = 1.0$ MN/m<br>$k_{x2} = k_{y2} = 1.3$ MN/m<br>$c_{x1} = c_{x2} = 0.1$ kNs/m<br>$c_{y1} = c_{y2} = 0.3$ kNs/m |
| Viscoelastic | **Case 1 (10% CIP)**<br>$k_\infty = 1.5$ MN/m<br>$\alpha = 10$<br>$\tau = 8.6667\text{x}10^{-4}$<br>$k_{MRE} = 0.1043$ MN/m @ 0 mT | **Case 2 (20% CIP)**<br>$k_\infty = 1.5$ MN/m<br>$\alpha = 1$<br>$\tau = 8.6667\text{x}10^{-3}$<br>$k_{MRE} = 0.1197$ MN/m @ 0 mT |

solutions of $\dot{\mathbf{x}}$ and $\dot{\mathbf{r}}$ depend on the rotor rotational speed for Eqs. (5.3) and (5.15) respectively. It is convenient to determine the way in which the roots change with the rotational speed graphically by plotting a Campbell diagram, where the rotational speed is on a horizontal axis and the natural frequencies on a vertical axis. By taking numerical data from [74], consider a uniform steel rigid rotor with density of 7810 kg/m$^3$, 0.5 m length, 0.2 m diameter and mounted on flexible supports. The rotor is located at the geometric centre of the system, 0.25 m from each support. From standard formulae for the mass, the polar and diametral moment of inertias of cylinder, the calculated value of corresponding mass is $m = 122.68$ kg, diametral moment of inertia is $I_d = 2.8625$ kgm$^2$ and polar moment of inertia is $I_p = 0.6134$ kgm$^2$. The parameter values for each support configuration are given in Table 5.1.

### 5.3.1 Free vibrations

An example of a rigid rotor mounted on uncoupled anisotropic bearings produces the natural frequency map shown in Figure 5.3a. By substituting the corresponding parameters into Equation (5.2), the coupling stiffnesses $k_{xC}$ and $k_{yC}$ are found to be zero. Thus, the first and second equations of Equation (5.1), for which all the right hand terms are neglected, are uncoupled from the main system and are independent of rotor angular speed, $\Omega$. Since the stiffnesses in both the horizontal and vertical directions are different, then the two natural frequencies that are determined from these equations in $x$ and $y$ are different. When the rotor is not rotating, the remaining two solutions of Equation (5.1) are also uncoupled with two distinct natural frequencies. However as the rotor speed increases the two equations are coupled by gyroscopic terms and one of the natural frequency is decreasing whilst the other is increasing. It can be seen that the

natural frequencies are converging on account of the gyroscopic effect. The decreasing line is one whereby the whirl is opposed to the rotor rotation direction, $\Omega$ and the increasing line is one where the whirl and the rotation directions, $\Omega$ are the same. The decreasing natural frequency also intersects with two constant natural frequencies lines at about 8000 and 13000 rev/min. This is a result of the equations of motion being uncoupled and independent of one another (i.e. $x$ and $\psi$ are uncoupled as the terms in the equations satisfy $k_{xC}x = k_{xC}\psi = 0$). The natural frequency map for a rigid rotor supported on coupled anisotropic bearings is depicted in Figure 5.3b. It can be seen from this figure that all of the natural frequency lines do not intersect, which imply all of the equations in Equation (5.1) are coupled. The two lower natural frequency lines exhibit mode veering as the lines exhibit sharp divergence [77] within the range of 10000 to 15000 rev/min.

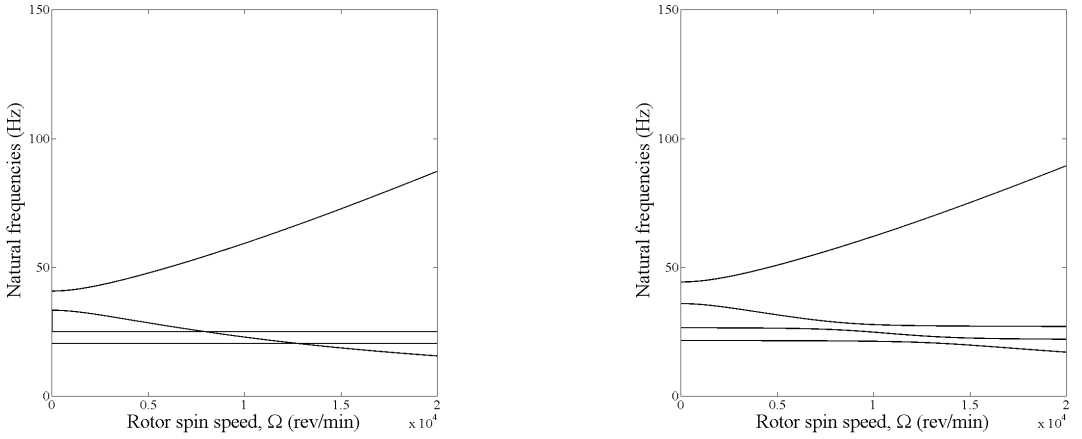


(a) Uncoupled system ($k_{iC} = 0$)

(b) Coupled system ($k_{iC} \neq 0$)

FIGURE 5.3: Natural frequency map for a rigid rotor mounted on flexible undamped supports. Cases (a) and (b) refer to a system with symmetric identical supports or different supports at the two ends respectively.

Figure 5.4 illustrates the mode shapes for a rigid rotor when the two support bearings are coupled anisotropic bearings, having the same parameters as in the example used for Figure 5.3b, at four different rotor speeds. The rotor displacement at both bearing locations are depicted. Solid lines connecting the two bearings are established by extending a straight line between each bearing at the same instant. For the first two modes, conical whirl can be observed for all of the rotor speeds except for the first mode at 10000 rev/min. The direction of the rotation is deduced by referring to Figure 5.4, where counterclockwise motion or forward whirl is positive rotation about the Z axis. However, cylindrical whirls occurred at all speeds, which are backward and forward whirl, for the third and fourth mode respectively except for third mode at 10000 rev/min.

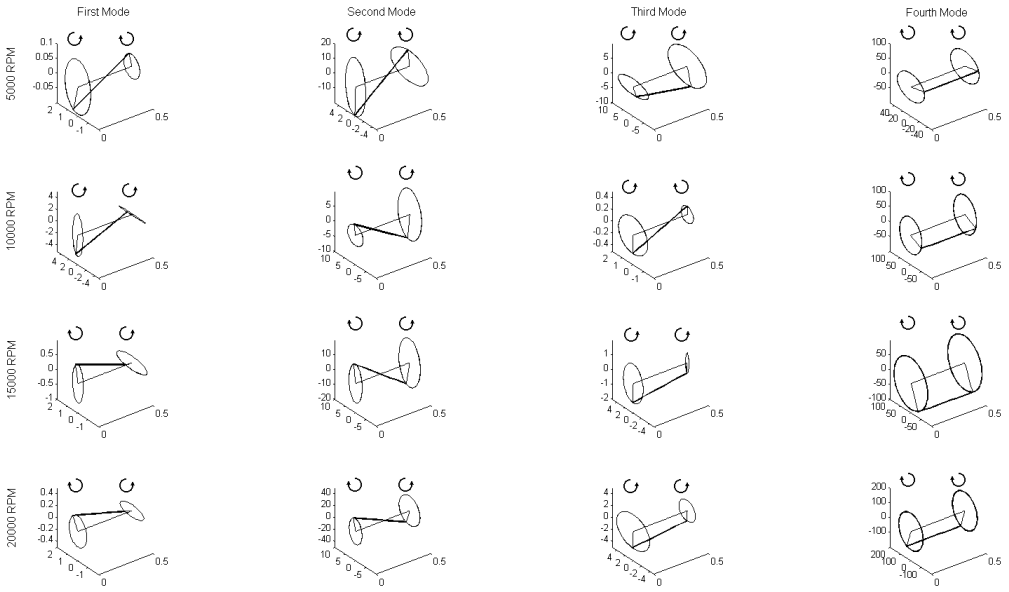


FIGURE 5.4: Mode shapes for a rigid rotor mounted on different undamped supports at the ends.

For cases of viscously damped supports, Figure 5.5 shows a comparison of two types of systems namely uncoupled and coupled systems. It can be seen that from case (a) of Figure 5.5a, two identical natural frequency lines result from solutions of the first and second equations of Equation (5.1) because of identical support stiffnesses in the $x$ and $y$ directions. A coupled system is observed in Figure 5.5b when all the coupling stiffness terms are not the same, which are obtained by substituting parameters from Table 5.1 into Equation 5.2. Thus the natural frequency lines do not intersect but mode veering [77] is observed for the second and third natural frequency lines.

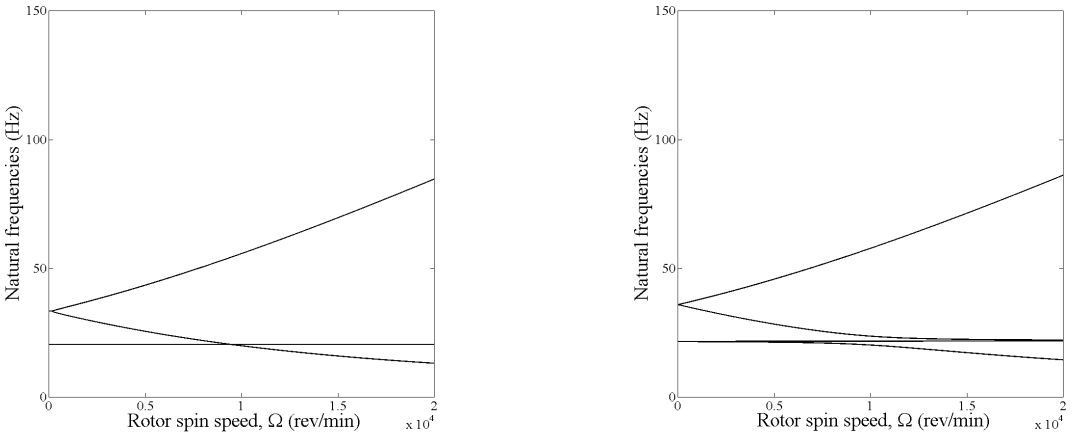


(a) Uncoupled system ($S_{iC} = 0$)

(b) Coupled system ($S_{iC} \neq 0$)

FIGURE 5.5: Natural frequency map for a rigid rotor mounted on isotropic viscously damped supports.

For the next example, identical viscoelastic supports are consider at both ends of the shaft where the properties of the material are assumed to be identical in both the $x$ and $y$ directions. Thus is similar to case (a) for viscously damped supports, which have identical stiffnesses in both horizontal and vertical directions at both support ends. Figures 5.6a and 5.6b show three different natural frequency lines. From Equation (5.11), the first two equations are uncoupled due to the position of the rotor being at the middle of the shaft. Thus the natural frequencies derived from these two equations are identical and independent of $\Omega$. Specifically for Case 1 as shown in Figure 5.6a, the lines of constant natural frequency intersect with a decreasing natural frequency line at about 16000 rev/min. Therefore the first and second equations of Equation (5.11) are uncoupled from the third and fourth. For Case 2 as in Figure 5.6b, two distinct natural frequency lines converge as the rotor speed increases due to the gyroscopic terms in the third and fourth equations of Equation (5.11). Even though both Case 1 and 2 are similar to case (a) for viscously damped supports in term of identical stiffnesses, the influence of the damping coefficients play an important role in influencing the behaviour of the natural frequencies changing over the range of rotor rotational speed. From Equation (5.12) and (5.13), damping coefficients of $\tau\alpha k_\infty$ are available in each equation of motion in Equation (5.12) by substituting every term of the internal variable of degree of freedom $p$.

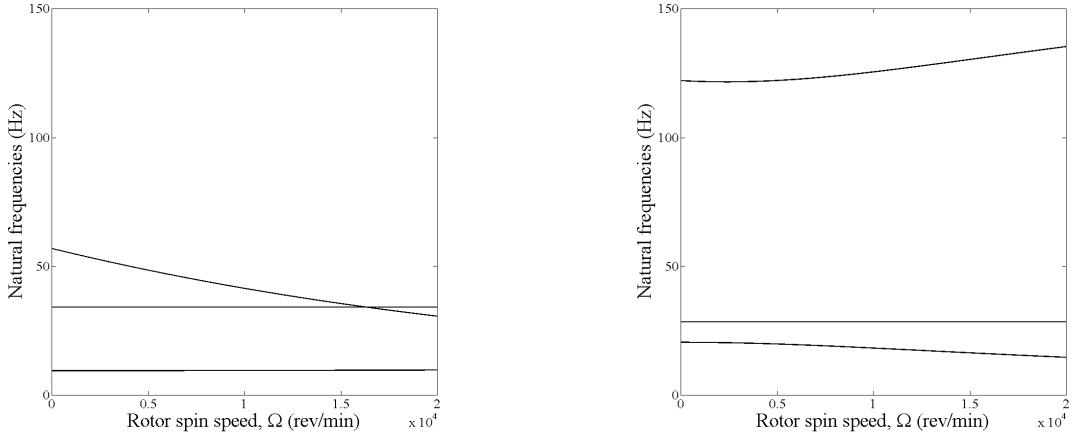


(a) Uncoupled system

(b) Coupled system

FIGURE 5.6: Natural frequency map for a rigid rotor mounted on identical isotropic viscoelastic supports.

### 5.3.2 Forced vibration

In this section, forced vibration analysis is demonstrated specifically for a rotor-bearing system mounted on identical viscoelastic supports, modelled by the standard linear type viscoelastic support with one internal variable.

Then the equations of motion including (5.13) are directly integrated using the Runge-Kutta method (available in MATLAB). Initial conditions for each integration of Eqs. (5.12) and (5.13) are set to zero including the value of $\delta$ and $\gamma$. Only rotor unbalance in the direction of $X$ and $Y$ is considered with the value of $\varepsilon = 1\text{x}10^{-4}$ m. In this analysis, the skewed centerline angle $\beta$ in third and fourth Equation (5.12) are not considered. The steady-state rotor response is obtained at specific rotor speed $\Omega$ after considering several thousands cycles of $t$ and plotted throughout certain range of $\Omega$. The response is defined by the $x$ and $y$ displacements of the rotor center and its magnitude is observed from the numerical analysis. Then results are presented by comparing the maximum magnitude response with associated loss factor of each pair of $\tau\alpha k_\infty$ and $\alpha k_\infty$ values.

For this simulations in this section, three cases that corresspond to pure silicone rubber, 10% MRE and 20% MRE. $k_\infty$, $\alpha$ and $\tau$ are referred to work by [76]. $k_\infty = 1.5$ MN/m and $\alpha = 1$ are applied to all cases. Meanwhile, $\tau$ values of $8.6667\text{x}10^{-5}$, $8.6667\text{x}10^{-4}$ and $8.6667\text{x}10^{-3}$ were assigned for 0% MRE, 10% MRE and 20% MRE respectively. Figures 5.7, 5.8 and 5.9 show the displacement magnitude responses of the rotor center and the corresponding modulus magnitude and loss factor for the three different samples of viscoelastic supports respectively. The associated dashed lines with similar colour legend indicates the frequency at which the loss factors are maximum. For both Case 0 and Case 1, the maximum magnitude of rotor center response are at much lower frequency than the corresponding dashed line where the frequencies for the maximum loss factor are 80060 rev/min and 8006 rev/min for Case 0 and Case 1 respectively. Resonant occurs at 1494 rev/min and 1504 rev/min for Case 0 and Case 1 respectively and its being indicated by a corresponding colour dot in both Figure 5.8 and 5.9. Reduction of maximum magnitude response is observed as $\tau$ is increased, but the most significant reduction can be seen for Case 2 where its maximum magnitude response, which is at 2039 rev/min located above its corresponding frequency of the maximum loss factor, 800 rev/min. Thus it is suggested that high damping behaviour and higher response attenuation are observed in the transition region of the viscoelastic material. By referring to Figure (2.1), the transition region is a region between rubbery and glassy, and it provides high damping behaviour. Thus the observation of higher response reduction when applying viscoelastic supports in rotor system is considered in good agreement within the transition region.

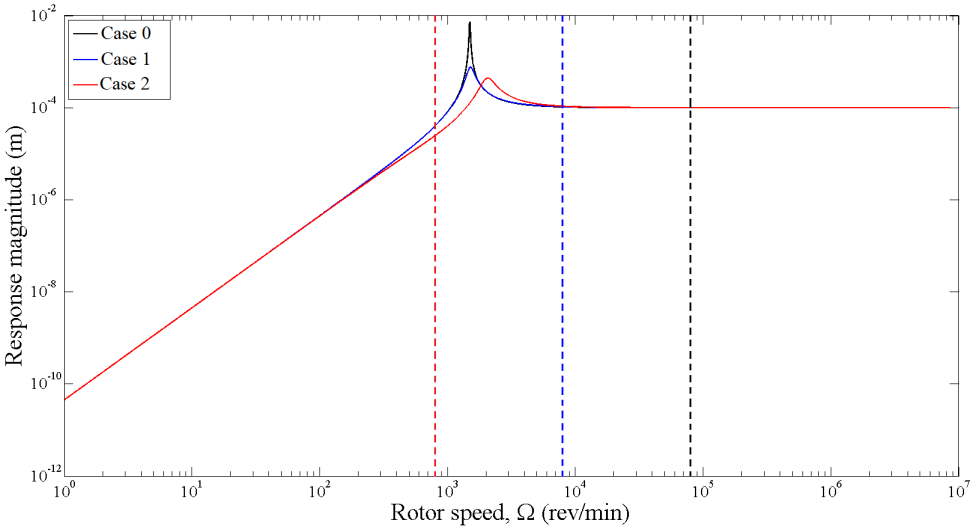


FIGURE 5.7: Magnitude of the rotor center displacement response of a rigid rotor mounted on three different viscoelastic supports at both shaft's ends (Case 0 = 0% MRE, Case 1 = 10% MRE, Case 20 = 0% MRE). The corresponding coloured dashed line are the frequencies of the maximum loss factor for each sample.

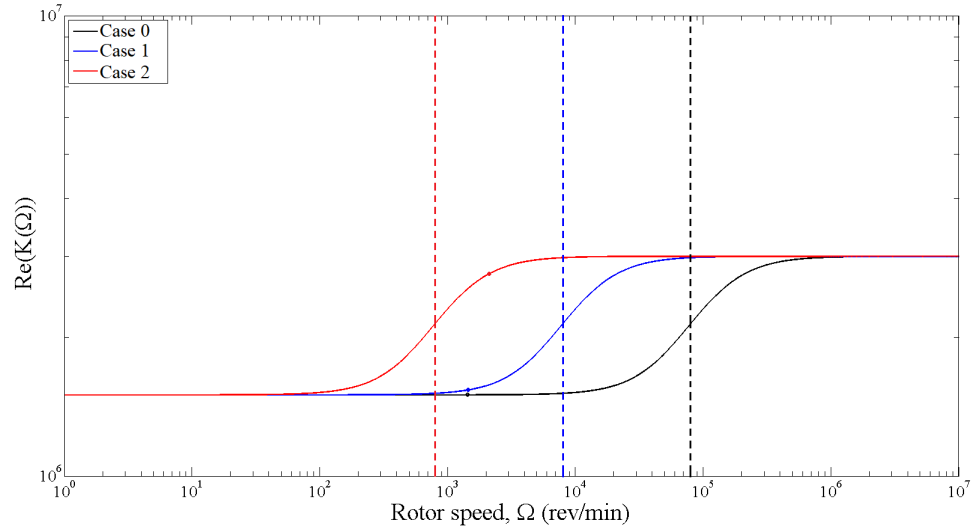


FIGURE 5.8: Magnitude of modulus, K($\omega$) of a rigid rotor mounted on three different viscoelastic supports (Case 0 = 0% MRE, Case 1 = 10% MRE, Case 20 = 0% MRE).

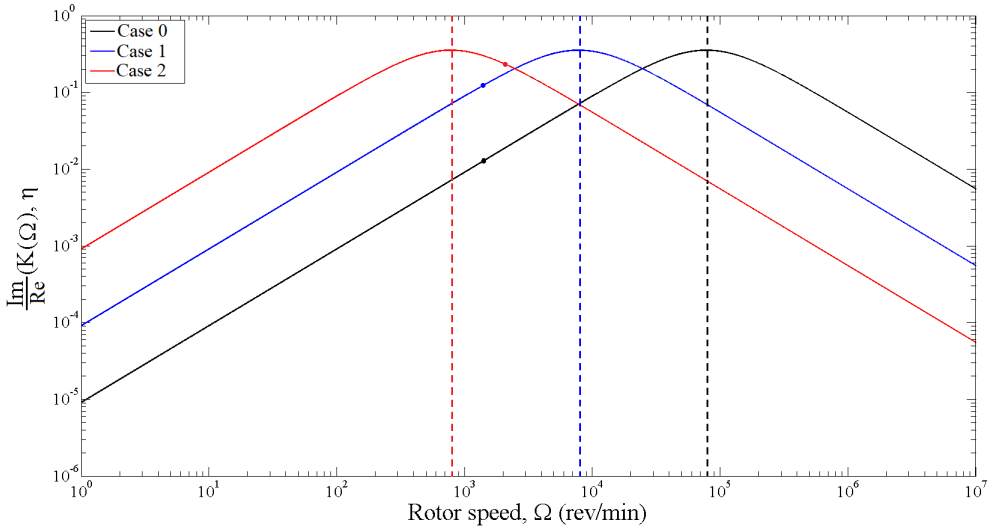


FIGURE 5.9: Loss factor of a rigid rotor mounted on three different viscoelastic supports (Case 0 = 0% MRE, Case 1 = 10% MRE, Case 20 = 0% MRE).

For the next simulation, a total of 100 pairs of $\alpha$ and $\tau$ are considered where 10 values of each $\alpha$ ranging from 1 to 10 and $\tau$ ranging from 8.6667x$10^{-4}$ to 8.6667x$10^{-3}$. Figure 5.10 depicts the surface plots of the maximum magnitude of the rotor centre and its corresponding resonance frequency. Each of the value is plotted against the pair of $\tau\alpha k_\infty$ and $\alpha k_\infty$ values which corresponds to the damping and stiffness coefficients in Figure 5.2 respectively. Stiffness value of $k_\infty$ is fix as in Table 5.1. It can be seen that from Figure 5.10a, in general, the maximum rotor center magnitude responses are decreasing when $\tau\alpha k_\infty$ increases for a specific value of $\alpha k_\infty$. However different observations are found as the stiffness component of $\alpha k_\infty$ is increased for each value of $\tau\alpha k_\infty$. This suggests the prominent effect of the damping element in the viscoelastic material for reducing the vibration level of the rotor motion. The corresponding resonance frequency at which maximum rotor response occurred is shown by Figure 5.10b. In general, again, increased values of $\tau\alpha k_\infty$ have a greater effect of shifting the resonance frequency to higher values compared to $\alpha k_\infty$, where the effect can only be seen for a medium to high range of $\tau\alpha k_\infty$.

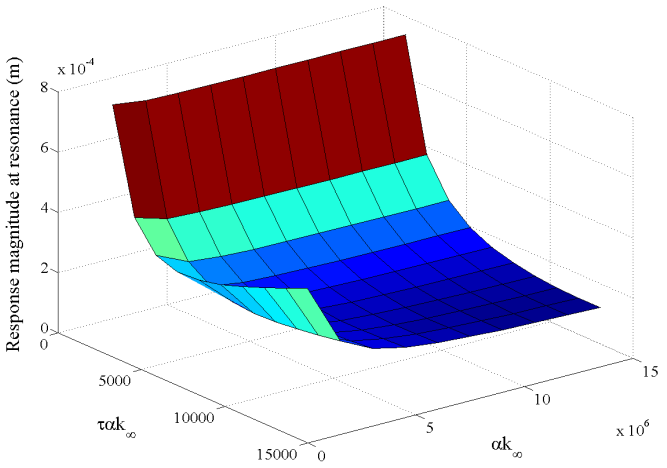


(a) Resonant response magnitude.

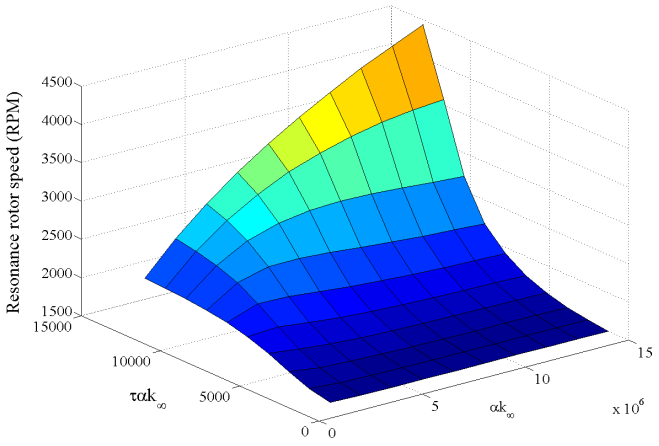


(b) Rotor speed for the resonant response.

FIGURE 5.10: Resonance speed and maximum displacement response magnitude for a rigid rotor mounted viscoelastic supports.

## 5.4 Conclusions

For the free vibration case, it can be concluded that the effect of the stiffness coefficients are dominant in determining the dynamics of the rotor for both the elastic and viscoelastic supports, which are explained by examination of the natural frequency maps. Specifically in terms of mode coupling, the stiffness is significant especially when the supports are not identical at both ends. The effect of the significant of gyroscopic moment is also observed as its produces the behaviour of diverging higher order natural frequencies.

For forced vibration case, the effect of damping is prominent. As the damping value of the standard linear model is increased, the attenuation of the rotor vibration response explicitly around the transition region of viscoelastic material is better. Furthermore, it also can provide a natural frequency shift. Because of that contribution and it is known

that viscoelastic materials have a complex stiffness property, they have possibility of having different behaviour over the range of frequency. Specifically in rotor-bearing system, by increasing the rotor spin speed to match or be around the transition frequency of the viscoelastic material is not a viable and easy approach as it may lead to other problem such as subsynchronous whirling. To ensure the capability of viscoelastic materials can be optimized, enhancement to its property can be made by transforming it into a smart material. By changing its complex stiffness property using external stimulation, so that it instantly shifts its transition frequency, the vibration response of rotor can be attenuated when the desired rotor speed falls in the transition region of the viscoelastic material. Thus, this possibility can be pursued by considering smart viscoelastic materials such as magnetorheological elastomer (MRE).

# Chapter 6

# Conclusions

To conclude this work, a common process of the fabrication of the isotropic MRE sample is presented. Starting from involved material and followed by mixing compound, manufacturing process until the testing procedure of the MRE sample. The type of material and the manufacturing process utilized in this chapter can be considered common aspects of which many researchers already implemented. Sample testing is, however, considering the availability of existing measurement device and faster measurement time, using a modal testing method. Utilization of impact hammer test with consideration of single-degree-of-freedom system, MRE stiffness and lost factor can be determined from accelerance and Nyquist plot respectively.

Then the linearised modulus MRE model, EMRE, comprises two components that are zero-field, $E_{mag0}$ and magnetic dependent property, $E_{mag}$ is considered. The zero-field property is defined by the series configuration of silicone rubber and CIP modulus and its corresponding volume percentage. The selection criteria of such configuration are due to the adequacy of the law of mixture that fits reasonably good with experimental results. Meanwhile, magnetic-field dependency properties of MRE under the compression is modelled by altering the shear model of dipole-dipole particle interaction. By considering small strain changes around an equilibrium state, the magnetic dependent modulus is linearly approximated by utilizing Taylor's series expansion of fifth order. Due to such approximation, this model is limited to linear elastic response and will not suitable for hardening of the MRE when a large magnetic field is induced. However, the linearised model, which can predict fairly accurate two sources of data from existing literature and experimental results from modal testing, can be beneficial for estimating MRE stiffness or modulus for different CIP concentration under the influence of the magnetic field. Theoretical estimation of the lower and upper range of MRE modulus can provide beneficial gain in switchable stiffness design later.

After that, the linearised MRE stiffness model is included in the standard linear model of viscoelastic to employ smart viscoelastic mounts in the simple rotor-bearing mathematical model. From the free vibration analysis, it can be concluded that the effect of the stiffness coefficients is dominant in determining the dynamics of the rotor for both the flexible and viscoelastic supports, which are explained by examination of the natural frequency maps. Specifically, in terms of mode coupling, the stiffness is significant especially when the supports are not identical at both ends. The effect of the signifcance of the gyroscopic moment is also observed as its produces the behaviour of diverging higher-order natural frequencies. For the forced vibration case, the effect of damping is prominent. As the damping value of the standard linear model is increased, the attenuation of the rotor vibration response explicitly around the transition region of viscoelastic material is better.

Furthermore, it also can provide a natural frequency shift. Because of that contribution and it is known that viscoelastic materials have a complex stiffness property, they have the possibility of having different behaviour over the range of frequency. Specifically in the rotor-bearing system, increasing the rotor spin speed to match or be around the transition frequency of the viscoelastic material is not a viable and easy approach as it may lead to other problem such as subsynchronous whirling. To ensure the capability of viscoelastic materials can be optimized, an enhancement to its property can be made by transforming it into a smart material. By changing its complex stiffness property using external stimulation, so that it instantly shifts its transition frequency, the vibration response of the rotor can be attenuated when the desired rotor speed falls in the transition region of the viscoelastic material.

**Future work and recommendation**

The work presented in this thesis uses a simplified rigid rotor model to represent rotating machinery. This model does not include the effect of shaft flexibility that commonly exists in most types of rotating machinery. The flexibility of the shaft gives rise to a bending natural frequency, which may influence the response of the rotor. It is recommended that the rotating machinery is represented with a single-mass flexible rotor in future work on the response of rotors supported by smart viscoelastic. As the linearised model of the MRE was fairly accurate in predicting the MRE modulus of previous researcher's works and data from modal testing, the simulated rotor response with MRE supports can be verified with lab-scale rotor rig. The rotor rig should comprises of MRE with similar size that utilized in the modal testing as the flexible supports. This work can be extended too by considering a control system of the rotor rig that utilize controllable magnetic field by inclusion of electromagnet. The setup of the electromagnet must take into account the proper electrical circuit, supplied voltage, the zero-field MRE modulus, useful range of MRE modulus change and the design of the electromagnet itself. A simple ON-OFF control strategy can be implemented by noting the required absolute change of MRE

modulus with respect of measured magnetic field and subsequently shift the rotor rig natural frequnecy at desired operating speed.

# Appendix A

# Derivation of Equation 5.11

The purpose of this appendix is to derive the final Equation 5.11 on Page 40. Details can be added to Figure 5.2 for deriving the reaction forces of the standard linear model. The details can be referred to Figure A1 below.

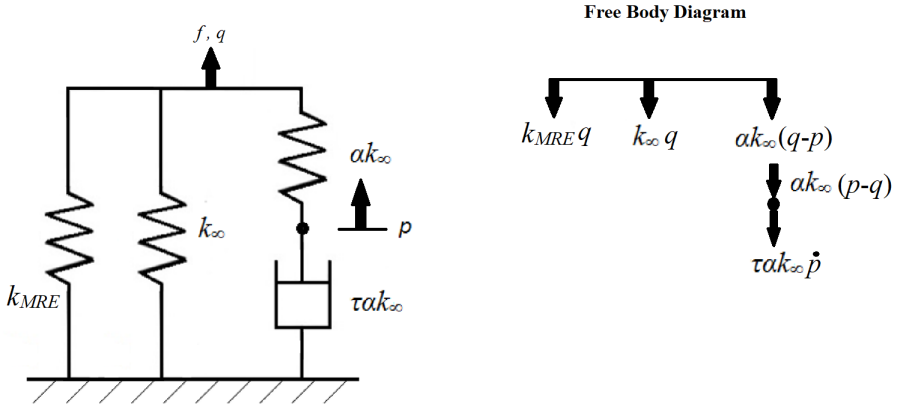


FIGURE A.1: Additional details on standard linear model of Figure 5.2 with corresponding free-body diagram.

Total reaction force, $f$, and its corresponding displacement, $q$, can be written as

$$f_q = \alpha k_\infty (q - p) + (k_\infty + k_{MRE})q \tag{A.1}$$

By referring to Figure 5.1, $x_1$ displacement can be expressed as

$$x_1 = x - a\psi \tag{A.2}$$

The $x_1$ displacement can be substituted into Equation A.1 as following

$$\begin{aligned} f_{x1} &= \alpha k_\infty (x - a\psi - p_{x1}) + (k_\infty + k_{MRE})(x - a\psi) \\ &= (k_{MRE} + k_\infty(1+\alpha))(x - a\psi) - k_\infty \alpha p_{x1} \end{aligned} \tag{A.3}$$

Similar approach can be adapted for $f_{x2}$, $f_{y1}$, and $f_{y2}$ by substituting respective displacements below

$$\begin{aligned} x_2 &= x + b\psi \\ y_1 &= y + a\theta \\ y_2 &= y - b\theta \end{aligned} \tag{A.4}$$

# Appendix B

# Derivation of Equation 5.12

This appendix will served as an example on how Equation 5.12 is obtained. Equation 5.12 signifies equations of motion for a rigid rotor mounted on identical viscoelastic supports. In this appendix, only $\ddot{x}$ will be shown. To account summation of forces in x-direction, the corresponding equation of motion can be written as

$$m\ddot{x} = -f_{x1} - f_{x2} + m\epsilon\Omega^2 \cos(\Omega t + \delta) \tag{B.1}$$

By substituting $f_{x1}$ and $f_{x2}$ from Equation 5.11 into Equation B.1, the equation of motion can be further written as

$$m\ddot{x} = -(k_\infty(1+\alpha) + k_{MRE})(2x - (a-b)\psi) + k_\infty\alpha(p_{x1} + p_{x2}) + m\epsilon\Omega^2 \cos(\Omega t + \delta) \tag{B.2}$$

To obtain final form as in Equation 5.12, these two terms which are $\hat{k} = k_\infty(1+\alpha)+k_{MRE}$ and $\hat{a} = k_\infty\alpha$ are introduced to Equation B.2. The the equation is divided by $m$ to give

$$\ddot{x} = -\frac{2\hat{k}}{m}x + \frac{\hat{k}(a-b)}{m}\psi + \frac{\hat{a}}{m}(p_{x1} + p_{x2}) + \epsilon\Omega^2 \cos(\Omega t + \delta) \tag{B.3}$$

# Bibliography


[1] A. D. Nashif and J. P. Henderson, *Vibration damping*. John Wiley & Sons, 1985.

[2] E. Rustighi, D. F. Ledezma-Ramirez, P. E. Tapia-Gonzalez, N. Ferguson, and A. Zakaria, "Modelling and experimental characterisation of a compressional adaptive magnetorheological elastomer isolator," *Journal of Vibration and Control*, p. 10775463211025336, 2021.

[3] G. Schubert, *Manufacture, characterisation and modelling of magneto-rheological elastomers*. PhD thesis, University of Glasgow, 2014.

[4] M. Kallio, *The elastic and damping properties of magnetorheological elastomers*. VTT Technical Research Centre of Finland, 2005.

[5] M. I. Friswell, J. T. Sawicki, D. Inman, and A. Lees, "The response of rotating machines on viscoelastic supports," *International Review of Mechanical Engineering*, vol. 1, no. 1, pp. 32–40, 2007.

[6] W. Rankine, "On the centrifugal force of rotating shafts," *Engineer*, vol. 27, p. 249, 1869.

[7] A. Dimarogonas, *Vibration for Engineers, 1996*. Prentice-Hall, Upper Saddle River, New Jersey.

[8] A. Richardson, *The evolution of the Parsons steam turbine*. Cambridge University Press, 2014.

[9] H. H. Jeffcott, "Xxvii. the lateral vibration of loaded shafts in the neighbourhood of a whirling speed. the effect of want of balance," *The London, Edinburgh, and Dublin Philosophical Magazine and Journal of Science*, vol. 37, no. 219, pp. 304–314, 1919.

[10] O. Reynolds, "'on the theory of lubrication and its application to mr. lowe's experiments,'," *Philos. Trans. R. Soc. London*, vol. 77, pp. 157–234, 1886.

[11] B. Newkirk and H. Taylor, "Shaft whipping due to oil action in journal bearings," *General Electric Review*, vol. 28, no. 8, pp. 559–568, 1925.

[12] A. Kimball, "Internal friction theory of shaft whirling," *General Electric Review*, vol. 27, no. 4, pp. 244–251, 1924.

[13] D. Smith, "The motion of a rotor carried by a flexible shaft in flexible bearings," *Proceedings of the Royal Society of London. Series A, Containing Papers of a Mathematical and Physical Character*, vol. 142, no. 846, pp. 92–118, 1933.

[14] J. Friedericy, R. Eppink, Y. Liu, and A. Cetiner, "An investigation of the behavior of floating ring dampers and the dynamics of hypercritical shafts on flexible supports," tech. rep., DTIC Document, 1965.

[15] S. Cooper, *Preliminary investigation of oil films for the control of vibration.* Institution of Mechanical Engineers, 1963.

[16] J. Vance, F. Zeidan, and B. Murphy, "History of machinery rotordynamics," *Machinery Vibration and Rotordynamics*, pp. 353–392, 2010.

[17] M. Stiassnie, "On the application of fractional calculus for the formulation of viscoelastic models," *Applied Mathematical Modelling*, vol. 3, no. 4, pp. 300–302, 1979.

[18] R. Fosdick and Y. Ketema, "A thermoviscoelastic dynamic vibration absorber," *Journal of applied mechanics*, vol. 65, no. 1, pp. 17–24, 1998.

[19] M. M. Sjöberg and L. Kari, "Non-linear behavior of a rubber isolator system using fractional derivatives," *Vehicle System Dynamics*, vol. 37, no. 3, pp. 217–236, 2002.

[20] K. Adolfsson, M. Enelund, and P. Olsson, "On the fractional order model of viscoelasticity," *Mechanics of Time-dependent materials*, vol. 9, no. 1, pp. 15–34, 2005.

[21] L. A. Silva, E. M. Austin, and D. J. Inman, "Time-varying controller for temperature-dependent viscoelasticity," *Journal of vibration and acoustics*, vol. 127, no. 3, pp. 215–222, 2005.

[22] N. Gil-Negrete, J. Vinolas, and L. Kari, "A nonlinear rubber material model combining fractional order viscoelasticity and amplitude dependent effects," *Journal of applied mechanics*, vol. 76, no. 1, p. 011009, 2009.

[23] J. Dutt and B. Nakra, "Stability characteristics of rotating systems with journal bearings on viscoelastic support," *Mechanism and machine theory*, vol. 31, no. 6, pp. 771–779, 1996.

[24] N. Shabaneh and J. W. Zu, "Dynamic analysis of rotor–shaft systems with viscoelastically supported bearings," *Mechanism and machine theory*, vol. 35, no. 9, pp. 1313–1330, 2000.

[25] H. G. Tillema, *Noise reduction of rotating machinery by viscoelastic bearing supports.* University of Twente, 2003.

[26] C. A. Bavastri, E. M. d. S. Ferreira, J. J. d. Espíndola, and E. M. d. O. Lopes, "Modeling of dynamic rotors with flexible bearings due to the use of viscoelastic materials," *Journal of the Brazilian Society of Mechanical Sciences and Engineering*, vol. 30, no. 1, pp. 22–29, 2008.

[27] Z. Rigbi and L. Jilken, "The response of an elastomer filled with soft ferrite to mechanical and magnetic influences," *Journal of magnetism and magnetic materials*, vol. 37, no. 3, pp. 267–276, 1983.

[28] I. Brigadnov and A. Dorfmann, "Mathematical modeling of magneto-sensitive elastomers," *International Journal of Solids and Structures*, vol. 40, no. 18, pp. 4659–4674, 2003.

[29] M. Lokander and B. Stenberg, "Performance of isotropic magnetorheological rubber materials," *Polymer Testing*, vol. 22, no. 3, pp. 245–251, 2003.

[30] P. Blom and L. Kari, "Amplitude and frequency dependence of magneto-sensitive rubber in a wide frequency range," *Polymer testing*, vol. 24, no. 5, pp. 656–662, 2005.

[31] Y. Wang, Y. Hu, L. Chen, X. Gong, W. Jiang, P. Zhang, and Z. Chen, "Effects of rubber/magnetic particle interactions on the performance of magnetorheological elastomers," *Polymer Testing*, vol. 25, no. 2, pp. 262–267, 2006.

[32] G. Stepanov, S. Abramchuk, D. Grishin, L. Nikitin, E. Y. Kramarenko, and A. Khokhlov, "Effect of a homogeneous magnetic field on the viscoelastic behavior of magnetic elastomers," *Polymer*, vol. 48, no. 2, pp. 488–495, 2007.

[33] L. Chen, X. Gong, and W. Li, "Effect of carbon black on the mechanical performances of magnetorheological elastomers," *Polymer testing*, vol. 27, no. 3, pp. 340–345, 2008.

[34] H.-X. Deng and X.-L. Gong, "Application of magnetorheological elastomer to vibration absorber," *Communications in nonlinear science and numerical simulation*, vol. 13, no. 9, pp. 1938–1947, 2008.

[35] J. Li, X. Gong, H. Zhu, and W. Jiang, "Influence of particle coating on dynamic mechanical behaviors of magnetorheological elastomers," *Polymer Testing*, vol. 28, no. 3, pp. 331–337, 2009.

[36] P. Blom and L. Kari, "The frequency, amplitude and magnetic field dependent torsional stiffness of a magneto-sensitive rubber bushing," *International Journal of Mechanical Sciences*, vol. 60, no. 1, pp. 54–58, 2012.

[37] J. Lejon and L. Kari, "Measurements on the temperature, dynamic strain amplitude and magnetic field strength dependence of the dynamic shear modulus of magnetosensitive elastomers in a wide frequency range," *Journal of Vibration and Acoustics*, vol. 135, no. 6, p. 064506, 2013.

[38] F. Sakly and M. Chouchane, "Vibration control of a rotor using smart bearings with magneto-rheological elastomer supports," in *International Conference on Advanced Materials Mechanics & Manufacturing*, pp. 376–382, Springer, 2021.

[39] J. Yao, Y. Gao, J. Fan, F. Scarpa, and Y. Li, "Design and verification of a magnetorheological elastomer-based actuator to reduce rotor vibration," *International Journal of Mechanics and Materials in Design*, pp. 1–18, 2022.

[40] M. R. Jolly, J. D. Carlson, B. C. Muñoz, and T. A. Bullions, "The magnetoviscoelastic response of elastomer composites consisting of ferrous particles embedded in a polymer matrix," *Journal of Intelligent Material Systems and Structures*, vol. 7, no. 6, pp. 613–622, 1996.

[41] L. Davis, "Model of magnetorheological elastomers," *Journal of Applied Physics*, vol. 85, no. 6, pp. 3348–3351, 1999.

[42] Y. Shen, M. F. Golnaraghi, and G. Heppler, "Experimental research and modeling of magnetorheological elastomers," *Journal of Intelligent Material Systems and Structures*, vol. 15, no. 1, pp. 27–35, 2004.

[43] L. Borcea and O. Bruno, "On the magneto-elastic properties of elastomer–ferromagnet composites," *Journal of the Mechanics and Physics of Solids*, vol. 49, no. 12, pp. 2877–2919, 2001.

[44] H. Yin, L. Sun, and J. Chen, "Micromechanics-based hyperelastic constitutive modeling of magnetostrictive particle-filled elastomers," *Mechanics of materials*, vol. 34, no. 8, pp. 505–516, 2002.

[45] D. Wang, J.-S. Chen, and L. Sun, "Homogenization of magnetostrictive particle-filled elastomers using an interface-enriched reproducing kernel particle method," *Finite elements in Analysis and Design*, vol. 39, no. 8, pp. 765–782, 2003.

[46] A. Dorfmann and R. Ogden, "Nonlinear magnetoelastic deformations of elastomers," *Acta Mechanica*, vol. 167, no. 1-2, pp. 13–28, 2004.

[47] H. Yin and L. Sun, "Magnetoelasticity of chain-structured ferromagnetic composites," *Applied Physics Letters*, vol. 86, no. 26, p. 261901, 2005.

[48] H. Yin, L. Sun, and J. Chen, "Magneto-elastic modeling of composites containing chain-structured magnetostrictive particles," *Journal of the Mechanics and Physics of Solids*, vol. 54, no. 5, pp. 975–1003, 2006.

[49] R. Bustamante, "Transversely isotropic nonlinear magneto-active elastomers," *Acta mechanica*, vol. 210, no. 3-4, pp. 183–214, 2010.

[50] P. P. Castañeda and E. Galipeau, "Homogenization-based constitutive models for magnetorheological elastomers at finite strain," *Journal of the Mechanics and Physics of Solids*, vol. 59, no. 2, pp. 194–215, 2011.

[51] K. Danas, S. Kankanala, and N. Triantafyllidis, "Experiments and modeling of iron-particle-filled magnetorheological elastomers," *Journal of the Mechanics and Physics of Solids*, vol. 60, no. 1, pp. 120–138, 2012.

[52] Y. Han, W. Hong, and L. E. Faidley, "Field-stiffening effect of magneto-rheological elastomers," *International Journal of Solids and Structures*, vol. 50, no. 14, pp. 2281–2288, 2013.

[53] L. Chen and S. Jerrams, "A rheological model of the dynamic behavior of magnetorheological elastomers," *Journal of Applied Physics*, vol. 110, no. 1, p. 013513, 2011.

[54] R. Li and L. Sun, "Dynamic viscoelastic modeling of magnetorheological elastomers," *Acta Mechanica*, vol. 225, no. 4-5, pp. 1347–1359, 2014.

[55] S. Opie and W. Yim, "A tunable vibration isolator using a magnetorheological elastomer with a field induced modulus bias," in *ASME 2007 International Mechanical Engineering Congress and Exposition*, pp. 99–104, American Society of Mechanical Engineers, 2007.

[56] W. J. Choi, *Dynamic analysis of magnetorheological elastomer configured sandwich structures*. PhD thesis, University of Southampton, 2009.

[57] M. Yu and S. Wang, "The composite mre embedded with a copper coil," *Smart Materials and structures*, vol. 19, no. 6, p. 065023, 2010.

[58] P. Zając, J. Kaleta, D. Lewandowski, and A. Gasperowicz, "Isotropic magnetorheological elastomers with thermoplastic matrices: structure, damping properties and testing," *Smart Materials and Structures*, vol. 19, no. 4, p. 045014, 2010.

[59] G. Hu, M. Guo, W. Li, H. Du, and G. Alici, "Experimental investigation of the vibration characteristics of a magnetorheological elastomer sandwich beam under non-homogeneous small magnetic fields," *Smart materials and structures*, vol. 20, no. 12, p. 127001, 2011.

[60] Z. Varga, G. Filipcsei, and M. Zrínyi, "Magnetic field sensitive functional elastomers with tuneable elastic modulus," *Polymer*, vol. 47, no. 1, pp. 227–233, 2006.

[61] A. Boczkowska, S. F. Awietjan, and R. Wroblewski, "Microstructure–property relationships of urethane magnetorheological elastomers," *Smart Materials and Structures*, vol. 16, no. 5, p. 1924, 2007.

[62] Í. Guðmundsson, "A feasibility study of magnetorheological elastomers for a potential application in prosthetic devices," 2011.

[63] F. Gordaninejad, X. Wang, and P. Mysore, "Behavior of thick magnetorheological elastomers," *Journal of Intelligent Material Systems and Structures*, vol. 23, no. 9, pp. 1033–1039, 2012.

[64] C. Bellan and G. Bossis, "Field dependence of viscoelastic properties of mr elastomers," *International Journal of Modern Physics B*, vol. 16, no. 17n18, pp. 2447–2453, 2002.

[65] Y. Li, J. Li, W. Li, and H. Du, "A state-of-the-art review on magnetorheological elastomer devices," *Smart Materials and Structures*, vol. 23, no. 12, p. 123001, 2014.

[66] J. L. Leblanc, "Rubber–filler interactions and rheological properties in filled compounds," *Progress in polymer science*, vol. 27, no. 4, pp. 627–687, 2002.

[67] J. D. Carlson and M. R. Jolly, "Mr fluid, foam and elastomer devices," *mechatronics*, vol. 10, no. 4, pp. 555–569, 2000.

[68] I. Standard and B. ISO, "Rubber, vulcanized or thermoplastic—determination of tensile stress-strain properties," 2005.

[69] S. R. Singiresu *et al.*, *Mechanical vibrations*. Addison Wesley Boston, MA, 1995.

[70] D. Ewins, "Modal testing: theory, practice and application (mechanical engineering research studies: engineering dynamics series)," *Research studies Pre, 2nd ed., ISBN-13*, pp. 978–0863802188, 2000.

[71] J. M. Ginder, M. E. Nichols, L. D. Elie, and J. L. Tardiff, "Magnetorheological elastomers: properties and applications," in *1999 Symposium on Smart Structures and Materials*, pp. 131–138, International Society for Optics and Photonics, 1999.

[72] S. Demchuk and V. Kuz'min, "Viscoelastic properties of magnetorheological elastomers in the regime of dynamic deformation," *Journal of Engineering Physics and Thermophysics*, vol. 75, no. 2, pp. 396–400, 2002.

[73] R. E. Rosensweig, *Ferrohydrodynamics*. Courier Corporation, 2013.

[74] M. I. Friswell, *Dynamics of rotating machines*. Cambridge University Press, 2010.

[75] J. M. Kelly and D. Konstantinidis, *Mechanics of rubber bearings for seismic and vibration isolation*. John Wiley & Sons, 2011.

[76] L. A. Silva, "Internal variable and temperature modeling behavior of viscoelastic structures–a control analysis," 2003.

[77] S. Vidoli and F. Vestroni, "Veering phenomena in systems with gyroscopic coupling," *Journal of applied mechanics*, vol. 72, no. 5, pp. 641–647, 2005.